Numerical Methods for Partial Differential Equations

WILEY

RESEARCH ARTICLE

Central Compact Finite-Difference Scheme With High Spectral Resolution for KdV Equation

Lavanya V. Salian[1] | Rathan Samala[1] | Debojyoti Ghosh[2]

[1]Department of Humanities and Sciences, Indian Institute of Petroleum and Energy, Visakhapatnam, India | [2]Center for Applied Scientific Computing, Lawrence Livermore National Laboratory, Livermore, California, USA

Correspondence: Rathan Samala (rathans.math@iipe.ac.in)

Received: 19 March 2025 | **Revised:** 2 October 2025 | **Accepted:** 4 November 2025

Keywords: accuracy | cell-node and cell-centered compact schemes | dispersive PDEs | Fourier analysis | KdV equation | spectral properties

ABSTRACT

This work presents a combination of cell-node and cell-centered compact finite difference scheme for the approximation of third derivatives involved in Korteweg–de Vries (KdV) equations. This approach employs a half-shifted derivative construction at cell centers, avoiding the need for compact interpolation, thereby removing transfer errors; hence, it improves spectral resolution and maintains high-order accuracy. Fourier analysis is performed to show the spectral properties of the proposed formulation, which provides higher spectral resolutions as compared to node-based compact schemes. A filtering strategy is incorporated to suppress high-frequency oscillations without compromising the accuracy of the numerical scheme, and the total variation diminishing Runge Kutta (TVDRK3) method is applied for time integration. Numerical experiments on linear, nonlinear, and coupled KdV systems are conducted, and a comparative analysis with cell-node compact schemes confirms that the proposed scheme consistently reduces errors by up to an order of magnitude and achieves high spectral resolution properties.

1 | Introduction

High-order compact finite difference schemes have emerged as essential tools for the accurate numerical solution of partial differential equations involving higher-order spatial derivatives, particularly in problems characterized by multiscale dynamics [1]. Of particular importance is the precise approximation of third-order derivatives, which play a central role in dispersive wave equations of the form

$$u_t + g(u)_x + f(u)_{xxx} = 0 \tag{1.1}$$

where the third-order spatial derivative term $f(u)_{xxx}$ captures the dispersive effects that balance nonlinear steepening represented by $g(u)_x$. This subtle interplay between nonlinearity and dispersion gives rise to remarkable wave phenomena, including the formation and propagation of solitary wave solutions that maintain their shape over extended distances [2, 3]. Among dispersive models, the Korteweg–de Vries (KdV) equation is a canonical example, extensively studied for its ability to describe nonlinear wave propagation in a wide range of physical contexts. These include shallow water dynamics [4], plasma physics [5], optical communication systems [6], semiconductor device modeling [7], aeroacoustics [8, 9], electromagnetic simulations [10], and tectonic processes [11]. Challenges arise in convection-dominated scenarios, where the coefficients of the third-derivative terms may be small or even zero. Accurate simulation of such equations requires spatial discretizations that not only achieve high formal order but also retain spectral-like fidelity across a broad range of wavenumbers.

The significance of the dispersive KdV equation and its applications has motivated the development of a variety of analytical and numerical approaches such as differential quadrature

method [12], the inverse scattering transform [13], and the variational iteration method (VIM) introduced by Wazwaz [14] to address problems involving the Burgers', cubic Boussinesq, KdV, and K(2, 2) equations. Furthermore, numerical strategies such as the local discontinuous Galerkin method [15], adaptive mesh refinement (AMR)-based line methods [16], and high-order compact schemes coupled with low-pass filters [17] have been successfully applied. More recently, weighted essentially non-oscillatory (WENO) schemes have been explored, including variants based on polynomial bases [18] and on exponential bases [19].

In this work, we focus on higher-order schemes and review the available literature on finite difference methods and their compact variants. High-order finite difference (FD) methods are broadly classified into explicit and compact (Padé-type) schemes. Explicit schemes use wide stencils whose size grows with accuracy, whereas compact schemes employ narrow stencils but require solving linear systems. Although compact schemes achieve a spectral-like resolution and higher accuracy [1], they involve additional complexity due to matrix inversions. Classical compact schemes, pioneered by Lele [1], have been extensively applied to the approximation of first-, second-, and third-order derivatives. Their effectiveness comes from the ability to achieve a spectral-like resolution using narrow stencils, which offers an optimal balance between efficiency and accuracy. However, existing approaches encounter certain limitations, such as

- cell-node compact schemes achieve good accuracy but suffer from reduced resolution at short wavelengths;
- cell-centered compact schemes attempt to improve resolution but introduce interpolation steps between staggered grids [20, 21], leading to transfer errors that degrade accuracy and stability.

Further, compact schemes have been explored with a combination of weighted essentially non-oscillatory schemes [22] to improve solution near discontinuities, but they suffer from a complex algorithmic structure, hence increasing computational cost. Another disadvantage with higher-order schemes is that they often suffer from high-frequency noise, generated by discretization errors and nonlinear interactions, which can contaminate the solution and induce numerical instabilities. To mitigate this issue, spatial filtering techniques have been widely developed and applied. Lele [1] introduced systematic low-pass spatial filters that suppress spurious oscillations while preserving solution accuracy. Among these, Padé-type implicit filters offer greater selectivity than explicit alternatives, enabling precise control of spectral properties. The effectiveness of such filters depends on their order, cutoff frequency, and the frequency of application during time integration.

Recent advances in central compact schemes have demonstrated approaches that incorporate both cell-node and cell-center information, which can significantly enhance spectral properties. Liu et al. [23] proposed a compact scheme for first derivatives that combines cell-centered and cell-node values, improving accuracy, formal order, and wave resolution without additional computational cost, though at the expense of increased memory usage. Wang et al. [24] extended this idea to second-order spatial derivatives within the acoustic wave equation, equating weighted summations computed on both cell nodes and centers, and leveraging Taylor series expansions and optimization-based techniques. Motivated by these works [23, 24], the present study develops a cell-centered compact scheme for third derivatives in KdV equations, which is first reported in the literature to the best of the authors' knowledge.

The methodology of this work is as follows: We develop a combination of cell-node and cell-centered compact schemes for third-derivatives with an enhanced spectral resolution for the KdV equations, termed as third-derivative central compact schemes (TDCCS). Our approach uses function values at both the cell-nodes and cell-centers to calculate third-order spatial derivatives at the cell-nodes. The cell-centered values are treated as independent variables and are evolved alongside the cell-node values. We determine spatial derivatives at the cell-centers by *half-shifting* formula initially developed for the cell-nodes. This approach slightly increases memory usage, but it does not add to the computational cost because the compact interpolation for half-grid values is replaced by a compact derivative formula applied at the half-grid points. Fourier analysis is performed to establish the spectral properties of the proposed schemes, highlighting their superior accuracy and improved resolution characteristics. Numerical experiments with some benchmark problems, including both one and two-dimensional scalar equations and an Ito-type coupled nonlinear system, are conducted to validate the theoretical predictions of the proposed schemes. A comparative analysis is performed to demonstrate the accuracy and robustness of the proposed scheme with TDCNCS, along with low-pass filters that suppress undesirable high-frequency instabilities without affecting the remaining components of the solution.

The structure of this paper is outlined as follows: Section 2 begins with a review of third derivative cell-node and cell-centered compact finite difference schemes. In Section 3, we present the derivation of the new scheme, providing detailed insights into the approach for determining the FD coefficients. In Section 4, a Fourier analysis is conducted to systematically evaluate the wave resolution of the proposed schemes. Section 5 briefly introduces the high-order low-pass filtering scheme employed to mitigate numerical oscillations. Section 6 presents time integration and linear stability analysis. In Section 7, numerical examples are presented to validate the advantages of the proposed method. In Section 8, we provide some concluding remarks.

2 | Cell-Node and Cell-Centered Compact Schemes

We begin by examining Lele's cell-node compact scheme, initially designed to achieve accuracy up to sixth-order in approximating the third derivative. In this section, we expand Lele's work in two aspects. First, we enhance the cell-node compact scheme, achieving an improved tenth-order accuracy. Secondly, we extend it to the cell-centered compact scheme with an accuracy of up to tenth-order.

We consider numerical approximations to the 1D prototypical dispersion equations of the form

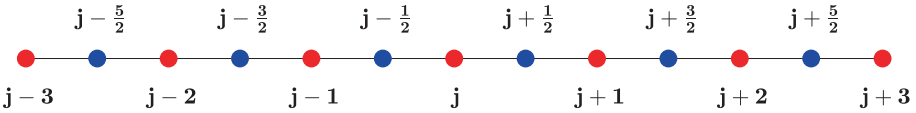

FIGURE 1 | The stencil of cell-center and cell-node compact schemes. The cell nodes and cell-centers are denoted by the red circles and blue circles, respectively.

TABLE 1 | The coefficients of TDCNCS schemes.

Scheme	a	b	c	α	β	Order
TDCNCS-E2	1	0	0	0	0	2
TDCNCS-E4	2	−1	0	0	0	4
TDCNCS-E6	$\frac{169}{60}$	$-\frac{12}{5}$	$\frac{7}{12}$	0	0	6
TDCNCS-T4	2	0	0	$\frac{1}{2}$	0	4
TDCNCS-T6	2	$-\frac{1}{8}$	0	$\frac{7}{16}$	0	6
TDCNCS-T8	$\frac{2367}{1180}$	$-\frac{167}{1180}$	$\frac{1}{236}$	$\frac{205}{472}$	0	8
TDCNCS-P6	$\frac{40}{21}$	0	0	$\frac{4}{9}$	$\frac{1}{126}$	6
TDCNCS-P8	$\frac{160}{83}$	$-\frac{5}{166}$	0	$\frac{147}{332}$	$-\frac{1}{166}$	8
TDCNCS-P10	$\frac{18221}{5478}$	$-\frac{1846}{913}$	$\frac{5}{66}$	$\frac{799}{2739}$	$-\frac{557}{5478}$	10

$$\frac{\partial u}{\partial t}+\frac{\partial g(u)}{\partial x}+\frac{\partial^3 f(u)}{\partial x^3}=0. \tag{2.1}$$

The framework for describing a semidiscrete finite difference is given by

$$\frac{du_j}{dt}=-g'_j-f'''_j. \tag{2.2}$$

Here, g'_j and f'''_j represent approximations to the spatial derivatives $\frac{\partial g(u)}{\partial x}$ and $\frac{\partial^3 f(u)}{\partial x^3}$ at the grid node x_j respectively. The computational domain is discretized uniformly into N points: $x_1, x_2, \ldots, x_{j-1}, x_j, x_{j+1}, \ldots, x_N$. The mesh size is denoted as $\Delta x = x_{j+1} - x_j$.

Figure 1 illustrates the stencil of cell nodes and the cell centers. For the computation of the first derivatives g'_j, the cell node compact scheme introduced by Lele [1] and the central compact scheme proposed by Liu et al. [23] are referenced. The linear cell-node compact scheme with up to sixth-order accuracy [1] is given by

$$\begin{aligned}&\beta f'''_{j-2}+\alpha f'''_{j-1}+f'''_j+\alpha f'''_{j+1}+\beta f'''_{j+2}\\&=a\frac{f_{j+2}-2f_{j+1}+2f_{j-1}-f_{j-2}}{2\Delta x^3}\\&\quad+b\frac{f_{j+3}-3f_{j+1}+3f_{j-1}-f_{j-3}}{8\Delta x^3}.\end{aligned} \tag{2.3}$$

We have extended the expression (2.3) to achieve up to tenth-order accuracy, denoted as the third derivative cell-node compact scheme (TDCNCS). The general form is given by

$$\begin{aligned}&\beta f'''_{j-2}+\alpha f'''_{j-1}+f'''_j+\alpha f'''_{j+1}+\beta f'''_{j+2}\\&=a\frac{f_{j+2}-2f_{j+1}+2f_{j-1}-f_{j-2}}{2\Delta x^3}\\&\quad+b\frac{f_{j+3}-3f_{j+1}+3f_{j-1}-f_{j-3}}{8\Delta x^3}\\&\quad+c\frac{f_{j+4}-4f_{j+1}+4f_{j-1}-f_{j-4}}{20\Delta x^3}.\end{aligned} \tag{2.4}$$

The third derivative cell-centered compact scheme (TDCCCS) is given by

$$\begin{aligned}&\beta f'''_{j-2}+\alpha f'''_{j-1}+f'''_j+\alpha f'''_{j+1}+\beta f'''_{j+2}\\&=a\frac{f_{j+\frac{3}{2}}-3f_{j+\frac{1}{2}}+3f_{j-\frac{1}{2}}-f_{j-\frac{3}{2}}}{\Delta x^3}\\&\quad+b\frac{f_{j+\frac{5}{2}}-5f_{j+\frac{1}{2}}+5f_{j-\frac{1}{2}}-f_{j-\frac{5}{2}}}{5\Delta x^3}\\&\quad+c\frac{f_{j+\frac{7}{2}}-7f_{j+\frac{1}{2}}+7f_{j-\frac{1}{2}}-f_{j-\frac{7}{2}}}{14\Delta x^3}.\end{aligned} \tag{2.5}$$

The left-hand sides of both Equations (2.4) and (2.5) involve spatial derivatives f'''_j computed at the grid nodes. While the right-hand side of equation (2.4) relies solely on function values f'''_j at the grid node x_j, Equation (2.5) incorporates function values $f_{j+\frac{1}{2}}$ at the center $x_{j+\frac{1}{2}}=\frac{1}{2}(x_j+x_{j+1})$ within each interval $x\in[x_j, x_{j+1}]$. The accuracy of these schemes is contingent upon specific choices for the coefficients (α, β, a, b, c). By matching terms in the Taylor series expansion around the point x_j, we can derive conditions for achieving different orders of accuracy. Tables 1 and 2 explicitly list the coefficients for the TDCNCS and TDCCCS schemes, respectively. By restricting the parameter $\alpha=\beta=0$, we obtain a family of explicit schemes. Further, setting $\alpha\neq 0$ and $\beta=0$ yields tridiagonal schemes. The combination of $\alpha\neq 0$ and $\beta\neq 0$ produces pentadiagonal schemes. These three distinct categories are referred to as TDCNCS-E, TDCNCS-T, and TDCNCS-P, respectively. Their formal order of accuracy is appended to their names for convenient identification. The truncation error for eighth-order accuracy is expressed as $Qf_j^{(11)}(x)\Delta x^8+\mathcal{O}(\Delta x^{10})$, where Q is 3.12192×10^{-5} for Equation (2.4) and 6.57252×10^{-5} for Equation (2.5).

Fourier analysis serves as an effective means for evaluating the accuracy and resolution characteristics of an FD scheme. The modified wavenumbers associated with the third-order spatial

TABLE 2 | The coefficients of TDCCCS schemes.

Scheme	a	b	c	α	β	Order
TDCCCS-E2	1	0	0	0	0	2
TDCCCS-E4	$\frac{13}{8}$	$-\frac{5}{8}$	0	0	0	4
TDCCCS-E6	$\frac{1299}{640}$	$-\frac{499}{384}$	$\frac{259}{960}$	0	0	6
TDCCCS-T4	$\frac{4}{3}$	0	0	$\frac{1}{6}$	0	4
TDCCCS-T6	$\frac{205}{166}$	$\frac{35}{166}$	0	$\frac{37}{166}$	0	6
TDCCCS-T8	$\frac{1058279}{975200}$	$\frac{96627}{195040}$	$-\frac{24787}{487600}$	$\frac{3229}{12190}$	0	8
TDCCCS-P6	$\frac{320}{233}$	0	0	$\frac{134}{699}$	$-\frac{7}{1398}$	6
TDCCCS-P8	$\frac{49720}{79903}$	$\frac{91400}{79903}$	0	$\frac{28838}{79903}$	$\frac{3541}{159806}$	8
TDCCCS-P10	$\frac{55463611}{150617762}$	$\frac{677644345}{451853286}$	$\frac{6301771}{225926643}$	$\frac{93443398}{225926643}$	$\frac{15505921}{451853286}$	10

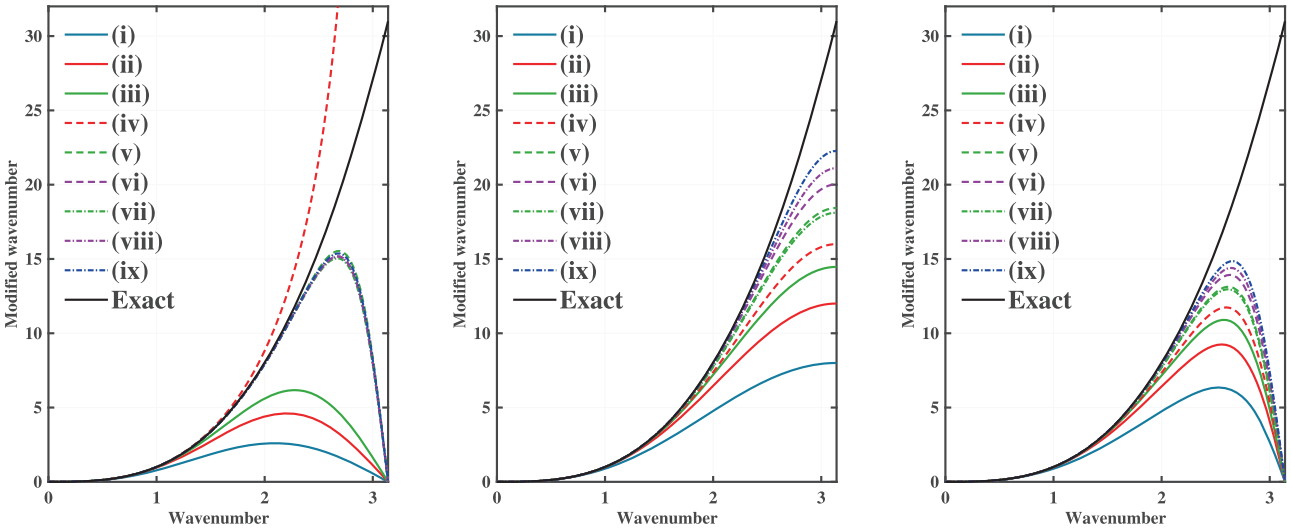

(a) TDCNCS (b) TDCCCS (c) TDCCCS-CI

FIGURE 2 | Plot of modified wavenumber vs. wavenumber for (a) TDCNCS, (b) TDCCCS, and (c) TDCCCS-CI: (i) E2; (ii) E4; (iii) E6; (iv) T4; (v) T6; (vi) T8; (vii) P6; (viii) P8; and (ix) P10. The tenth-order pentadiagonal scheme is adopted for the compact interpolation in TDCCCS-CI.

derivative for Equations (2.4) and (2.5) are

$$\omega'''_{\text{TDCNCS}} = \frac{a[2\sin(\omega)-\sin(2\omega)] + \frac{b}{4}[3\sin(\omega)-\sin(3\omega)] + \frac{c}{10}[4\sin(\omega)-\sin(4\omega)]}{1+2\alpha\cos(\omega)+2\beta\cos(2\omega)}, \tag{2.6}$$

$$\omega'''_{\text{TDCCCS}} = \frac{2a[3\sin(\frac{\omega}{2})-\sin(\frac{3\omega}{2})] + \frac{2b}{5}[5\sin(\frac{\omega}{2})-\sin(\frac{5\omega}{2})] + \frac{c}{7}[7\sin(\frac{\omega}{2})-\sin(\frac{7\omega}{2})]}{1+2\alpha\cos(\omega)+2\beta\cos(2\omega)}. \tag{2.7}$$

Here, the parameter $\omega = k\Delta x$ represents the scaled wavenumber, and ω''' signifies the scaled modified wavenumber. Exact difference approximation occurs when the scaled wavenumber ω and the scaled modified wavenumber ω''' coincide, as represented by the equation $\omega = \omega'''$.

Figure 2 illustrates the plot of modified wavenumber vs. wavenumber, representing the resolution properties for various schemes: (a) TDCNCS, (b) TDCCCS. The schemes include (i) second-order explicit scheme (E2), (ii) fourth-order explicit scheme (E4), (iii) sixth-order explicit scheme (E6), (iv) fourth-order tridiagonal scheme (T4), (v) sixth-order tridiagonal scheme (T6), (vi) eighth-order tridiagonal scheme (T8), (vii) sixth-order pentadiagonal scheme (P6), (viii) eighth-order pentadiagonal scheme (P8), and (ix) tenth-order pentadiagonal scheme (P10). Notably, for the same operator length, TDCCCS exhibits significantly enhanced resolution compared to TDCNCS. However, the implementation of TDCCCS requires the estimation of function values at the cell centers. The high-order compact interpolation (CI) scheme represents the most straightforward method to perform this estimation,

$$\beta\hat{f}_{j-\frac{3}{2}} + \alpha\hat{f}_{j-\frac{1}{2}} + \hat{f}_{j+\frac{1}{2}} + \alpha\hat{f}_{j+\frac{3}{2}} + \beta\hat{f}_{j+\frac{5}{2}} = a\frac{f_{j+1}+f_j}{2} + b\frac{f_{j+2}+f_{j-1}}{2} + c\frac{f_{j+3}+f_{j-2}}{2}, \tag{2.8}$$

where $\hat{f}_{j+\frac{1}{2}}$ represent the interpolated values at the midpoints $(j+\frac{1}{2})$. The transfer function corresponding to (2.8) is

$$T_{\text{CI}}(\omega) = \frac{a\cos(\frac{\omega}{2}) + b\cos(\frac{3\omega}{2}) + c\cos(\frac{5\omega}{2})}{1+2\alpha\cos(\omega)+2\beta\cos(2\omega)}. \tag{2.9}$$

TABLE 3 | The coefficients of the transfer function.

Scheme	a	b	c	α	β	Order
CI-E2	1	0	0	0	0	2
CI-E4	$\frac{9}{8}$	$-\frac{1}{8}$	0	0	0	4
CI-E6	$\frac{75}{64}$	$-\frac{25}{128}$	$\frac{3}{128}$	0	0	6
CI-T4	$\frac{4}{3}$	0	0	$\frac{1}{6}$	0	4
CI-T6	$\frac{3}{2}$	$\frac{1}{10}$	0	$\frac{3}{10}$	0	6
CI-T8	$\frac{25}{16}$	$\frac{5}{32}$	$-\frac{1}{224}$	$\frac{5}{14}$	0	8
CI-P6	$\frac{64}{45}$	0	0	$\frac{2}{9}$	$-\frac{1}{90}$	6
CI-P8	$\frac{8}{5}$	$\frac{8}{35}$	0	$\frac{2}{5}$	$\frac{1}{70}$	8
CI-P10	$\frac{5}{3}$	$\frac{5}{14}$	$\frac{1}{126}$	$\frac{10}{21}$	$\frac{5}{126}$	10

The coefficients in Equation (2.8) can be determined by matching the truncated expansion (TE) coefficients corresponding to different orders of accuracy, which are listed in Table 3. We use the notation TDCCCS-CI to represent TDCCCS combined with the CI scheme. To achieve greater precision in the interpolated function values at the midpoints, a larger interpolation stencil is required, leading to an increased computational cost. In this study, we employ the tenth-order penta-diagonal CI scheme to calculate function values at the cell-centers within the framework of TDCCCS-CI. Figure 2c illustrates the dispersion relations of TDCCCS-CI for various accuracy levels. When compared to Figure 2b, it becomes evident that the use of CI results in a noticeable reduction in resolution for the TDCCCS, as it introduces transfer errors.

3 | Central Compact Schemes for Third-Derivatives

This section introduces the methodology for designing third derivative central compact schemes (TDCCS). The stencil in the cell-centered compact schemes, as defined by Equation (2.5), includes both grid points and half-grid points, denoted as $\{j-\frac{5}{2}, j-2, j-\frac{3}{2}, j-1, j-\frac{1}{2}, j, j+\frac{1}{2}, j+1, j+\frac{3}{2}, j+2, j+\frac{5}{2}\}$. However, only the values corresponding to the cell centers, specifically $\{j-\frac{5}{2}, j-\frac{3}{2}, j-\frac{1}{2}, j+\frac{1}{2}, j+\frac{3}{2}, j+\frac{5}{2}\}$, are utilized in computing derivatives at the cell nodes $\{j-2, j-1, j, j+1, j+2\}$. Employing both the values at the cell nodes $\{j-2, j-1, j, j+1, j+2\}$ and the cell centers $\{j-\frac{5}{2}, j-\frac{3}{2}, j-\frac{1}{2}, j+\frac{1}{2}, j+\frac{3}{2}, j+\frac{5}{2}\}$ could potentially result in a compact scheme with increased order accuracy and improved resolution [23, 24]. Inspired by this concept, we propose a new category of third derivative central compact schemes (TDCCS) represented by the following formula:

$$\begin{aligned}
&\beta f'''_{j-2} + \alpha f'''_{j-1} + f'''_j + \alpha f'''_{j+1} + \beta f'''_{j+2} \\
&= a\frac{4f_{j+1} - 8f_{j+\frac{1}{2}} + 8f_{j-\frac{1}{2}} - 4f_{j-1}}{\Delta x^3} \\
&\quad + b\frac{8f_{j+\frac{3}{2}} - 12f_{j+1} + 12f_{j-1} - 8f_{j-\frac{3}{2}}}{5\Delta x^3} \\
&\quad + c\frac{8f_{j+\frac{5}{2}} - 20f_{j+1} + 20f_{j-1} - 8f_{j-\frac{5}{2}}}{35\Delta x^3}.
\end{aligned} \tag{3.1}$$

Note that in Equation (3.1), we must initially compute the function values at the cell-centers. These values at the cell-centers can be determined using the high-order CI method, as described in Equation (2.8). Nevertheless, as previously discussed in the preceding section, employing the high-order CI approach may introduce transfer errors that undermine the precision of TDCCS. To ensure the accuracy of the cell-center values, the values at the cell centers are stored as independent computational variables, and the identical scheme is employed to compute updating values on cell nodes. This involves a straightforward approach by shifting the indices in Equation (3.1) by $\frac{1}{2}$.

$$\begin{aligned}
&\beta f'''_{j-\frac{5}{2}} + \alpha f'''_{j-\frac{3}{2}} + f'''_{j-\frac{1}{2}} + \alpha f'''_{j+\frac{1}{2}} + \beta f'''_{j+\frac{3}{2}} \\
&= a\frac{4f_{j+\frac{1}{2}} - 8f_j + 8f_{j-1} - 4f_{j-\frac{3}{2}}}{\Delta x^3} \\
&\quad + b\frac{8f_{j+1} - 12f_{j+\frac{1}{2}} + 12f_{j-\frac{3}{2}} - 8f_{j-2}}{5\Delta x^3} \\
&\quad + c\frac{8f_{j+2} - 20f_{j+\frac{1}{2}} + 20f_{j-\frac{3}{2}} - 8f_{j-3}}{35\Delta x^3}.
\end{aligned} \tag{3.2}$$

It is important to note that this modification results in a higher memory demand to store function values in cell centers. However, there is no corresponding increase in computational cost, as compact interpolation (2.8) is substituted with the comparable-cost compact updating (3.2). Both Equations (3.1) and (3.2), for the same accuracy order, utilize an identical set of coefficients. To derive the relationships among the coefficients a, b, c, α, and β in Equation (3.1), we match the Taylor series coefficients of different orders. Solving the resulting set of linear equations yields schemes ranging from second to tenth orders. The relationships for different orders are presented as follows.

Second order:

$$1 + 2\alpha + 2\beta = a + b + c \tag{3.3}$$

Fourth order:

$$\alpha + 2^2\beta = \frac{a}{16} + \frac{13b}{80} + \frac{29c}{80} \tag{3.4}$$

Sixth order:

$$\alpha + 2^4\beta = \frac{13a}{160} + \frac{93b}{160} + \frac{2451c}{1120} \tag{3.5}$$

Eighth order:

$$\alpha + 2^6\beta = \frac{205a}{2688} + \frac{4069b}{2688} + \frac{30025c}{2688} \tag{3.6}$$

TABLE 4 | The coefficients of TDCCS schemes.

Scheme	a	b	c	α	β	Order
TDCCS-E4	$\frac{13}{8}$	$-\frac{5}{8}$	0	0	0	4
TDCCS-E6	$\frac{361}{192}$	$-\frac{129}{128}$	$\frac{49}{384}$	0	0	6
TDCCS-T4	$\frac{8}{7}$	0	0	$\frac{1}{14}$	0	4
TDCCS-T6	5	−5	0	$-\frac{1}{2}$	0	6
TDCCS-T8	$\frac{58021}{14120}$	$-\frac{109007}{28240}$	$\frac{1029}{28240}$	$-\frac{1261}{3530}$	0	8
TDCCS-P6	$\frac{320}{273}$	0	0	$\frac{74}{819}$	$-\frac{1}{234}$	6
TDCCS-P8	$\frac{19640}{4621}$	$-\frac{353000}{87799}$	0	$-\frac{33746}{87799}$	$-\frac{147}{175598}$	8
TDCCS-P10	$\frac{74390155}{19635801}$	$-\frac{45752035}{13090534}$	$\frac{4684435}{39271602}$	$-\frac{5803114}{19635801}$	$\frac{74747}{39271602}$	10

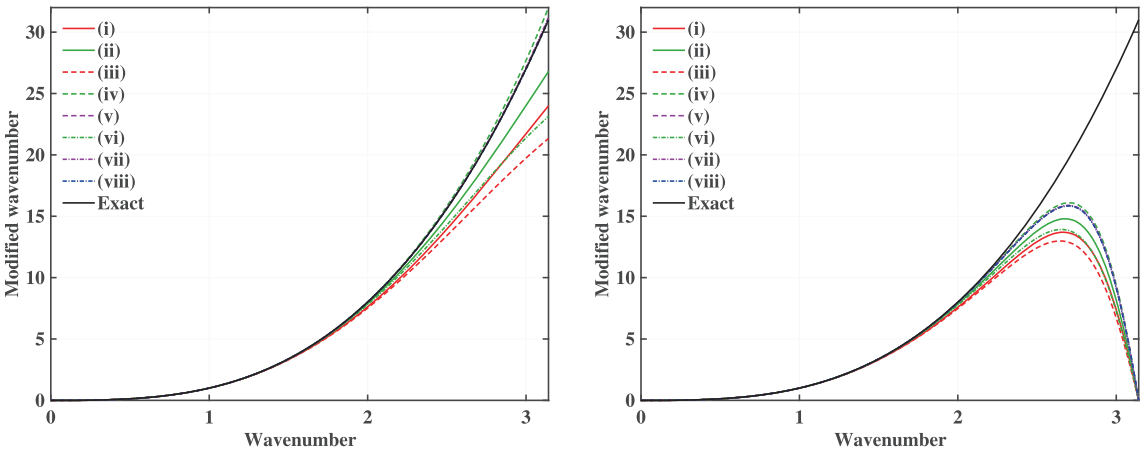

(a) TDCCS (b) TDCCS-CI

FIGURE 3 | Plot of modified wavenumber vs. wavenumber for (a) TDCCS, (b) TDCCS-CI: (i) E4; (ii) E6; (iii) T4; (iv) T6; (v) T8; (vi) P6; (vii) P8; and (viii) P10.

Tenth order:

$$\alpha + 2^8\beta = \frac{671a}{7680} + \frac{36991b}{7680} + \frac{534991c}{7680} \tag{3.7}$$

By solving Equations (3.3–3.7), we can determine the coefficients for TDCCS. When the schemes are constrained to $\alpha = \beta = 0$, they yield an explicit family of TDCCS. Conversely, if the schemes are limited to $\alpha \neq 0$, various tridiagonal TDCCS are derived. Moreover, when both $\alpha \neq 0$ and $\beta \neq 0$, the result is a family of pentadiagonal TDCCS. We label these three distinct types of schemes as TDCCS-E, TDCCS-T, and TDCCS-P, respectively. For ease of identification and unambiguous referencing, the formal order of accuracy of each scheme type is appended to its respective acronym. Table 4 presents the coefficients for TDCCS. The CCS-T6 and CCS-T8 schemes strike a remarkable balance between resolution, accuracy, and efficiency. They achieve sixth- and eighth-order accuracy, respectively, while maintaining a tridiagonal matrix structure, leading to significant computational savings compared to pentadiagonal schemes with equivalent accuracy. For the latter numerical analysis, we are considering eighth-order TDCCS. The truncation error for eighth-order accuracy TDCCS (3.1) is given by $2.1882 \times 10^{-6} f_j^{(11)}(x)\Delta x^8 + \mathcal{O}(\Delta x^{10})$. Note that the magnitude of the leading error term in the TDCCS scheme is an order of magnitude lower than the corresponding TDCNCS scheme of the same order.

4 | Fourier Analysis of the Errors

The main incentive behind developing TDCCS schemes is to precisely resolve small scales in multiscale physical problems. Consequently, Fourier analysis is conducted on these optimal schemes to evaluate their spectral characteristics. In this section, we investigate the dispersion and dissipation properties of TDCCS through Fourier analysis. TDCCS, being a central difference, eliminates numerically dissipative errors. The Fourier transformation, a frequently employed tool in finite difference scheme analysis, is applied to Equation (2.5), and by utilizing Euler's formula, the modified wavenumber ω''' of TDCCS can be derived. It is

$$\omega'''_{\text{TDCCS}} = \frac{\begin{array}{c}2a[8\sin(\frac{\omega}{2}) - 4\sin(\omega)] + \frac{2b}{5}[12\sin(\omega) - 8\sin(\frac{3\omega}{2})] \\ + \frac{2c}{35}[20\sin(\omega) - 8\sin(\frac{5\omega}{2})]\end{array}}{1 + 2\alpha\cos(\omega) + 2\beta\cos(2\omega)}. \tag{4.1}$$

Here, ω represents the scaled wavenumber with $\omega = k\Delta x$, and ω''' represents the scaled modified wavenumber.

Figure 3 shows plots comparing modified wavenumber vs. wavenumber for third derivative approximations using different methods: (a) The Taylor expansion-based method (TDCCS) and (b) the tenth-order pentadiagonal compact interpolation (TDCCS-CI). The schemes encompass various orders and types, including (i) fourth-order explicit scheme (E4), (ii)

TABLE 5 | The shortest well-resolved wave ω_f and resolving efficiency e of different schemes with tolerance error $\epsilon_t = 0.001$.

	4-T		6-T		8-T		10-P	
Schemes/order	ω_f	e	ω_f	e	ω_f	e	ω_f	e
TDCNCS	0.693	0.2205	1.735	0.5523	1.576	0.5018	1.635	0.5205
TDCCCS	0.716	0.2278	1.164	0.3705	1.468	0.4672	1.845	0.5874
TDCCCS-CI	0.715	0.2277	1.162	0.3699	1.445	0.4600	1.682	0.5354
TDCCS-CI	0.722	0.2297	2.037	0.6483	1.769	0.5631	1.748	0.5565
TDCCS	0.722	0.2297	1.386	0.4411	2.459	0.7828	2.998	0.9542

TABLE 6 | The shortest well-resolved wave ω_f and resolving efficiency e of different schemes with tolerance error $\epsilon_t = 0.0001$.

	4-T		6-T		8-T		10-P	
Schemes/order	ω_f	e	ω_f	e	ω_f	e	ω_f	e
TDCNCS	0.392	0.1248	1.524	0.4850	1.211	0.3855	1.293	0.4114
TDCCCS	0.405	0.1290	0.800	0.2545	1.105	0.3518	1.493	0.4753
TDCCCS-CI	0.405	0.1290	0.799	0.2544	1.097	0.3490	1.362	0.4336
TDCCS-CI	0.407	0.1294	1.994	0.6347	1.468	0.4672	1.420	0.4521
TDCCS	0.407	0.1294	0.785	0.2497	1.689	0.5376	2.288	0.7284

sixth-order explicit scheme (E6), (iii) fourth-order tridiagonal scheme (T4), (iv) sixth-order tridiagonal scheme (T6), (v) eighth-order tridiagonal scheme (T8), (vi) sixth-order pentadiagonal scheme (P6), (vii) eighth-order pentadiagonal scheme (P8), and (viii) tenth-order pentadiagonal scheme (P10). The resolutions achieved by TDCCS surpass those of TDCCCS and TDCNCS. The explicit TDCCS even has higher resolution than the tenth-order pentadiagonal TDCNCS, TDCCCS, and TDCCCS-CI. Hence, these schemes exhibit spectral-like resolution.

The bandwidth resolving efficiency [1] is a quantitative indicator of spectral resolution. The resolving efficiency of the FD scheme, with a specified error tolerance, is defined as

$$e = \frac{\omega_f}{\pi},$$

where ω_f is the shortest well-resolved wave component satisfying

$$\left|\frac{\omega'''(\omega) - \omega^3}{\omega^3}\right| \le \epsilon_t,$$

and ϵ_t represents the error tolerance threshold. This threshold remains constant when comparing various compact FD schemes. Tables 5 and 6 present the values of the bandwidth resolving efficiency (e) for various compact finite difference (FD) schemes, with error tolerances set at $\epsilon_t = 0.001$ and $\epsilon_t = 0.0001$, respectively. Tables 5 and 6 highlight that TDCCS exhibits the highest resolving efficiency, effectively capturing a broader range of wavenumbers under the same error tolerance. Specifically, for $\epsilon_t = 0.001$, the resolving efficiency of an eighth-order TDCNCS is 0.5018, while that of TDCCS is 0.7828. Similarly, for $\epsilon_t = 0.0001$, the resolving efficiency of an eighth-order TDCNCS is 0.3855, whereas that of TDCCS is 0.5376. Moreover, TDCCS is derived by evaluating the resolution efficiency for various possible combinations of cell nodes and cell centers, and it demonstrates the best performance among them, although the other combinations are not presented here.

5 | Low-Pass Spatial Filter

With high-order finite difference schemes, it is necessary to artificially mitigate all spurious waves while preserving the accuracy and resolution of the computed solution. This can be performed by regularizing the computed solution via a high-order low-pass spatial filter (LPSF) [1]. A tridiagonal filter of high order can be expressed as

$$\alpha_F \hat{f}_{j-1} + \hat{f}_j + \alpha_F \hat{f}_{j+1} = \sum_{n=0}^{N} \frac{a_n}{2}(f_{j+n} + f_{j-n}) \tag{5.1}$$

where f_j denotes the given value at point j, and $\hat{f}_j$ denotes the value after filtering. The transfer function corresponding to (5.1) is given by

$$T(\omega) = \frac{\sum_{n=0}^{N} a_n \cos(n\omega)}{1 + 2\alpha_F \cos(\omega)}. \tag{5.2}$$

To determine the unknown coefficients, we require the exclusion of the highest-frequency mode by imposing the condition $T(\pi) = 0$. For adaptability, we maintain α_F as an unrestricted parameter. Subsequently, the remaining N equations can be deduced by equating the Taylor series coefficients of the left and right sides. Through this process, Equation (5.1) yields a $2N$-th order formula within a $2N + 1$ point stencil. It is important to note that $T(\omega)$ is real, signifying that the filter alters only the amplitude of each wave component without impacting the phase. Here α_F is a free parameter that satisfies $|\alpha_F| < 0.5$. The coefficients of the 12th-order filter (F12) are given in the Table 7.

TABLE 7 | Coefficients for the filter formula.

Scheme	a_0	a_1	a_2	a_3	a_4	a_5	a_6	Order
F12	$\frac{(793+462\alpha_F)}{1024}$	$\frac{(99+314\alpha_F)}{256}$	$\frac{495(-1+2\alpha_F)}{2048}$	$\frac{55(1-2\alpha_F)}{512}$	$\frac{33(-1+2\alpha_F)}{1024}$	$\frac{3(1-2\alpha_F)}{512}$	$\frac{(-1+2\alpha_F)}{2048}$	12

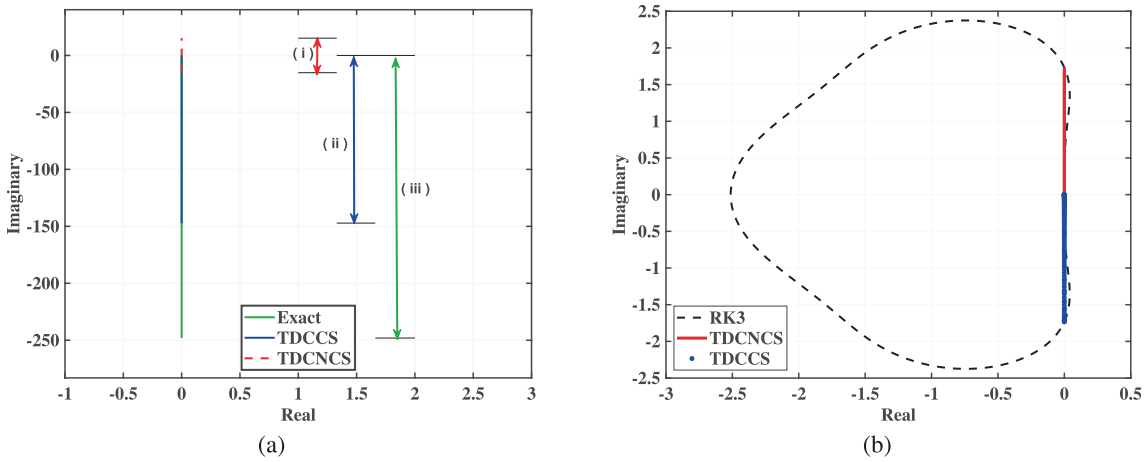

(a) (b)

FIGURE 4 | (a) Eigenvalues of the (i) Exact, (ii) TDCCS, and (iii) TDCNCS. (b) Stability regions of the three-stage Runge–Kutta time-integration scheme and eigenvalues of the TDCNCS and TDCCS scaled by their maximum stable CFL.

6 | Time Integration

Discretizing the spatial derivatives using the compact scheme described in Equations (3.1) and (3.2) yields an ordinary differential equation (ODE), given as

$$\frac{du}{dt} = S(u), \tag{6.1}$$

where $S(u)$ is the spatially-discretized approximation of the right-hand side. The ODE is evolved in time using the third-order TVD Runge–Kutta (TVDRK3) method [25]:

$$\begin{aligned} u^{(1)} &= u^n + \Delta t S(u^n), \\ u^{(2)} &= \frac{3}{4}u^n + \frac{1}{4}u^{(1)} + \frac{1}{4}\Delta t S(u^{(1)}), \\ u^{n+1} &= \frac{1}{3}u^n + \frac{2}{3}u^{(2)} + \frac{2}{3}\Delta t S(u^{(2)}). \end{aligned} \tag{6.2}$$

Figure 4a shows the eigenvalues of the exact, TDCNCS, and TDCCS schemes, while Figure 4b shows the stability region boundary of the TVDRK3 method. Linear stability requires a time step Δt such that the eigenvalues of the spatial discretization scheme scaled by $\Delta t/\Delta x^3$ fall within the stability region of the time integration method. Since the eigenvalues of the TDCNCS and TDCCS schemes are purely imaginary, we consider the value at which the stability region boundary of TVDRK3 intercepts the imaginary axis, i.e., ± 1.732. The maximum magnitude of the eigenvalues for the TDCNCS and TDCCS schemes are 15.157 and 147.168, respectively. This results in the following linear stability bound on the time step:

$$\frac{\Delta t}{\Delta x^3} \leq 0.11 \text{ (TDCNCS)}, \quad 0.011 \text{ (TDCCS)}. \tag{6.3}$$

Figure 4b shows the eigenvalues of the TDCNCS and TDCCS schemes scaled by these limits, and they lie within the stability region of TVDRK3. The TDCCS scheme has a very restrictive time step bound compared with the TDCNCS scheme, and this is a significant drawback. In future work, we propose to develop optimized high-order explicit Runge–Kutta methods for the TDCCS schemes [26] to allow larger time steps.

7 | Numerical Results

This section presents several numerical experiments that demonstrate the accuracy and effectiveness of the proposed method. The tests aim to highlight the high-order accuracy of the scheme for one-dimensional linear and nonlinear problems, as well as for a two-dimensional linear problem. In addition, the performance of the method is assessed in convection-dominated cases, particularly when the coefficients of the third-derivative terms are small. For problems involving both convection and dispersion, spatial discretization is performed using two high-order compact schemes for comparison:

- *TDCNCS*: The existing eighth-order cell-node compact scheme [1] for the first derivative, combined with the eighth-order cell-node compact schemes (2.4) for the third derivative,
- *TDCCS*: The existing eighth-order central compact scheme [23] for the first derivative, combined with the newly developed eighth-order cell-centered compact schemes (3.1) for the third derivative.

To quantify accuracy, the following error norms are employed:

$$L^\infty = \max_{0\leq i\leq N} |u_e - u_a|,$$

$$L^1 = \frac{1}{N+1}\sum_{i=0}^{N} |u_e - u_a|,$$

$$L^2 = \left(\frac{1}{N+1}\sum_{i=0}^{N} |u_e - u_a|^2\right)^{1/2},$$

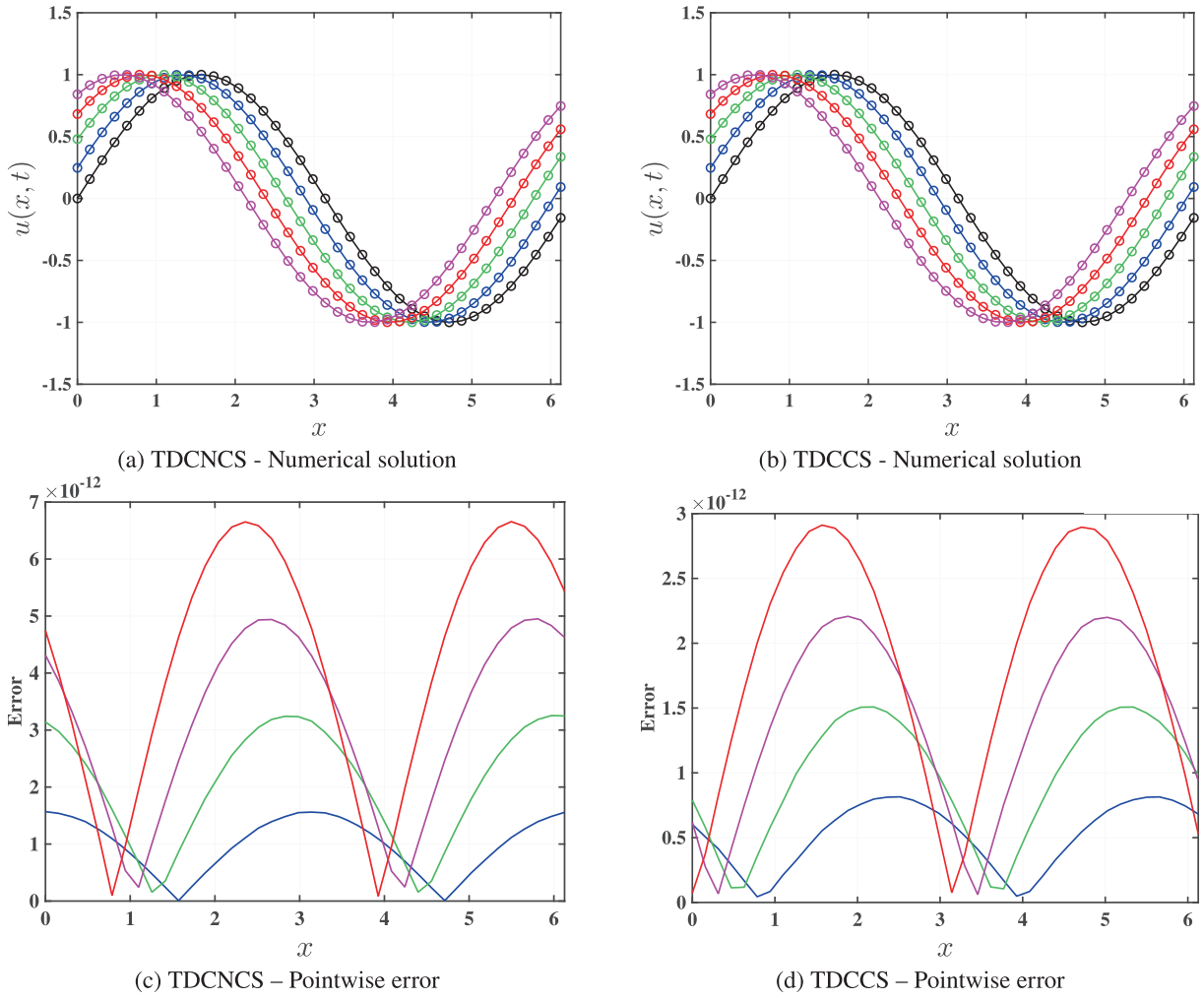

(a) TDCNCS - Numerical solution

(b) TDCCS - Numerical solution

(c) TDCNCS – Pointwise error

(d) TDCCS – Pointwise error

FIGURE 5 | Numerical results for Example 7.1 with $c = 1$. The first and second columns correspond to TDCNCS and TDCCS, respectively. The top row displays the exact solution (solid lines) and the numerical approximation (○) of the left-moving wave at $t = 0$ (black), $t = 0.25$ (blue), $t = 0.5$ (green), $t = 0.75$ (magenta), and $t = 1$ (red). The bottom row shows the associated pointwise errors, which grow with time.

where u_e and u_a denote the exact and approximate solutions, respectively. For stability in linear cases, the time step Δt is chosen using a CFL value of 0.01, computed as

$$\Delta t = \frac{0.01}{\left(\frac{\max|g'(u)|}{\Delta x} + \frac{\max|f'(u)|}{\Delta x^3}\right)}, \quad \text{(1D case)}, \tag{7.1}$$

and

$$\Delta t = \frac{0.01}{\left(\frac{\max|g_1'(u)|}{\Delta x} + \frac{\max|g_2'(u)|}{\Delta y} + \frac{\max|f_1'(u)|}{\Delta x^3} + \frac{\max|f_2'(u)|}{\Delta y^3}\right)}, \quad \text{(2D case)}. \tag{7.2}$$

The selected time step lies within the stability region of both TDCNCS and TDCCS schemes (see Equation 6.3), thereby guaranteeing numerical stability and physically meaningful results. Periodic boundary conditions are employed in all numerical experiments. All numerical experiments are performed on a MacBook Pro with an Apple M1 chip and 8 GB of memory, using MATLAB-R2024a.

Example 7.1. Consider the linear one-dimensional KdV equation

$$\begin{cases} u_t + c^{-2}u_{xxx} = 0, & (x,t) \in [0, 2\pi] \times [0, 1], \\ u(x, 0) = \sin(cx), & x \in [0, 2\pi], \end{cases} \tag{7.3}$$

whose exact solution is the left-moving wave $u(x, t) = \sin(c(x + t))$ for $x \in [0, 2\pi]$, $t \in [0, 1]$. Two representative cases are examined: A low wavenumber with $c = 1$ ($N = 40$, $k\Delta x = 0.157$) and a higher wavenumber with $c = 8$ ($N = 40$, $k\Delta x = 1.2566$).

For $c = 1$, the computed solutions and pointwise errors for $N = 40$ at $t = 0, 0.25, 0.5, 0.75, 1$ are shown in Figure 5, while Table 8 reports the L^∞-, L^1-, and L^2-errors together with the observed convergence rates at the final time $t = 1$. For example, the L^∞-error decreases from 1.6089×10^{-9} (TDCNCS) and 6.4028×10^{-10} (TDCCS) at $N = 20$ to 6.6573×10^{-12} and 2.9112×10^{-12}, respectively, at $N = 40$. Beyond this resolution, the error stagnates at machine precision.

For $c = 8$, the solutions and corresponding pointwise errors for $N = 40$ at $t = 0, 0.3, 0.7, 1$ are shown in Figure 6, with error

TABLE 8 | Errors and spatial order of convergence for Example 7.1 with $c = 1$ at $t = 1$.

Scheme	N	L^∞-error	Rate	L^1-error	Rate	L^2-error	Rate
TDCNCS ($c = 1$)	10	4.1920e-07	—	2.7131e-07	—	2.9230e-07	—
	20	1.6089e-09	8.0254	1.0249e-09	8.0483	1.1120e-09	8.0381
	30	6.2438e-11	8.0133	3.9824e-11	8.0103	4.3506e-11	7.9933
	40	6.6573e-12	7.7810	4.2273e-12	7.7965	4.6423e-12	7.7783
TDCCS ($c = 1$)	10	1.1729e-07	—	7.5910e-08	—	8.1641e-08	—
	20	6.4028e-10	7.5172	4.0809e-10	7.5393	4.4262e-10	7.5271
	30	2.6557e-11	7.8493	1.6932e-11	7.8485	1.8473e-11	7.8340
	40	2.9112e-12	7.6846	1.8481e-12	7.6996	2.0286e-12	7.6785

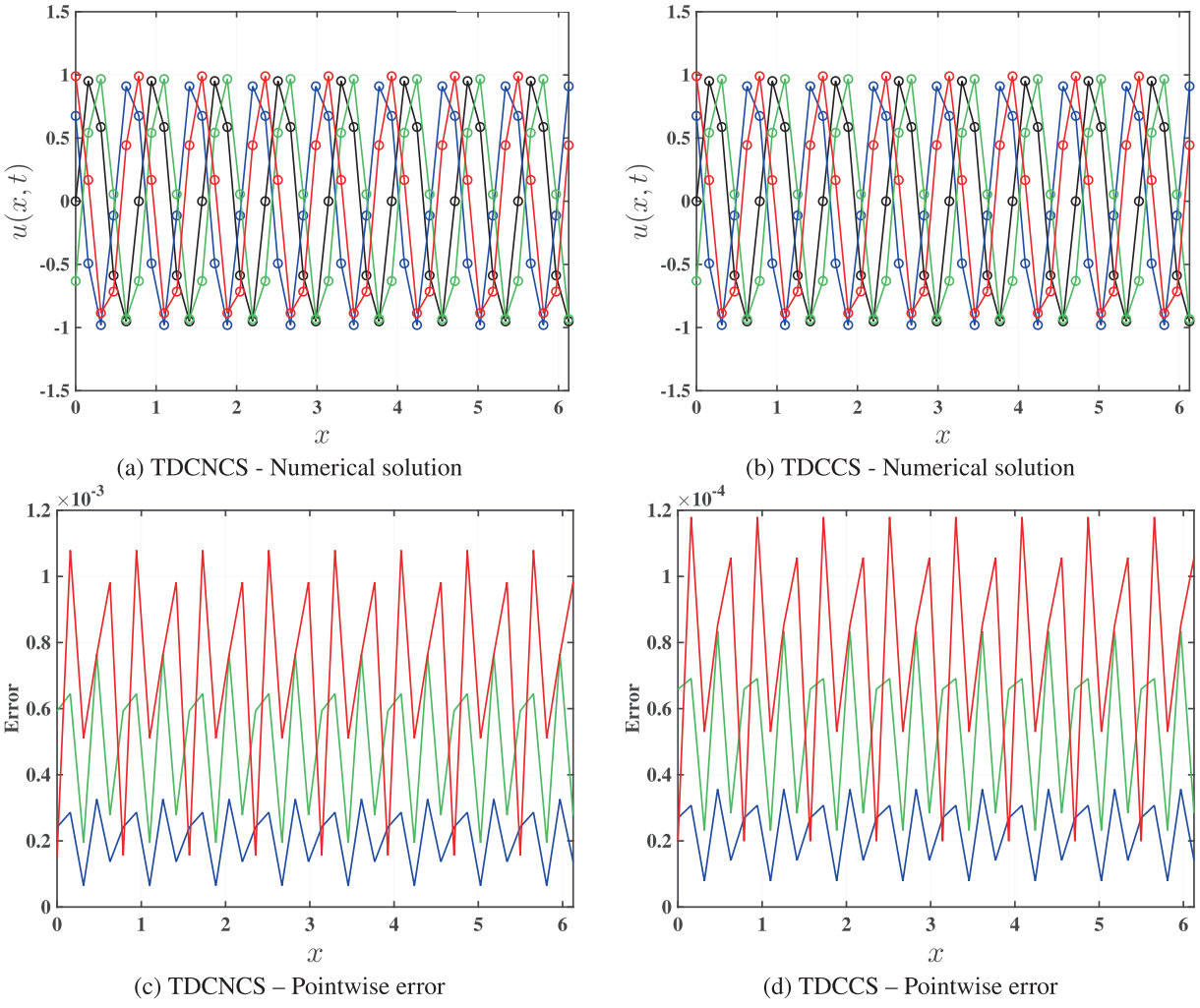

(a) TDCNCS - Numerical solution (b) TDCCS - Numerical solution

(c) TDCNCS – Pointwise error (d) TDCCS – Pointwise error

FIGURE 6 | Numerical results for Example 7.1 with $c = 8$. The first and second columns correspond to TDCNCS and TDCCS, respectively. The top row displays the exact solution (solid lines) and the numerical approximation (○) of the left-moving wave at $t = 0$ (black), $t = 0.3$ (blue), $t = 0.7$ (green), and $t = 1$ (red). The bottom row shows the associated pointwise errors, which increase over time.

metrics summarized in Table 9. In this setting, TDCCS consistently yields an order of magnitude lower absolute error compared to TDCNCS. For $N = 40$, the L^∞-error is 1.1×10^{-3} for TDCNCS vs. 1.1796×10^{-4} for TDCCS, while for $N = 160$, the errors reduce to 1.2758×10^{-8} and 5.0733×10^{-9}, respectively. Although both retain near-eighth-order accuracy, TDCCS achieves superior accuracy across all tested resolutions. Notably, no low-pass filtering is applied in these computations.

Example 7.2. To evaluate the method's accuracy in addressing nonlinear problems, we compute the classical soliton solution of the KdV equation.

TABLE 9 | Errors and spatial order of convergence for Example 7.1 with $c = 8$ at $t = 1$.

Scheme	N	L^∞-error	Rate	L^1-error	Rate	L^2-error	Rate
TDCNCS ($c = 8$)	20	7.9090e-01	—	5.1190e-01	—	5.4650e-01	—
	40	1.1000e-03	9.4898	6.9840e-04	9.5176	7.6483e-04	9.4809
	60	3.6490e-05	8.4003	2.3273e-05	8.3891	2.5610e-05	8.3772
	80	3.4187e-06	8.2305	2.2126e-06	8.1796	2.4374e-06	8.1759
	100	5.6757e-07	8.0471	3.6157e-07	8.1179	3.9972e-07	8.1021
	120	1.3032e-07	8.0702	8.3118e-08	8.0637	9.1845e-08	8.0663
	140	3.7705e-08	8.0454	2.4012e-08	8.0552	2.6569e-08	8.0464
	160	1.2758e-08	8.1152	8.2414e-09	8.0085	9.0886e-09	8.0335
TDCCS ($c = 8$)	20	9.4000e-03	—	6.1000e-03	—	6.5000e-03	—
	40	1.1796e-04	6.3163	7.6348e-05	6.3201	8.3279e-05	6.2863
	60	7.5773e-06	6.7705	4.8327e-06	6.8067	5.3206e-06	6.7838
	80	9.5592e-07	7.1963	6.1869e-07	7.1452	6.8076e-07	7.1472
	100	1.8591e-07	7.3379	1.1843e-07	7.4091	1.3090e-07	7.3889
	120	4.6895e-08	7.5545	2.9909e-08	7.5480	3.3055e-08	7.5485
	140	1.4411e-08	7.6543	9.1774e-09	7.6640	1.0155e-08	7.6562
	160	5.0733e-09	7.8184	3.2789e-09	7.7078	3.6158e-09	7.7334

$$\begin{cases} u_t - 3(u^2)_x + u_{xxx} = 0, & x \in [-10, 12], \quad t \geq 0, \\ u(x, 0) = -2\text{sech}^2(x), & x \in [-10, 12]. \end{cases} \tag{7.4}$$

The exact solution is $u(x, t) = -2\text{sech}^2(x - 4t)$ for $x \in [-10, 12]$ and $t \in [0, 0.5]$. Figure 7 presents the numerical solutions and corresponding errors for $N = 80$ at $t = 0, 0.25, 0.5$, while Table 10 lists the L^∞, L^1, and L^2 errors together with the observed convergence rates for grid sizes ranging from $N = 20$ to $N = 160$.

The results indicate that TDCCS provides consistently higher accuracy, with errors at least an order of magnitude smaller than those of TDCNCS for all tested grid sizes. The improved accuracy is accompanied by greater computational effort, as the runtime of TDCCS is more than twice that of TDCNCS. In terms of convergence, TDCCS approaches seventh-order accuracy for larger N, whereas TDCNCS maintains a rate close to the theoretical eighth order. For example, with $N = 160$, TDCNCS yields an error of 1.2705×10^{-7}, which is comparable to the error obtained by TDCCS at $N = 100$ under similar computational effort. Increasing the grid size beyond $N = 160$ does not lead to further error reduction due to machine precision limits. In summary, TDCCS delivers higher accuracy, while TDCNCS remains more efficient in terms of computational cost.

Example 7.3. We solve the following nonlinear KdV equations. To observe the effectiveness of our method in handling a nonlinear problem with a low coefficient for the third derivative term, we calculate the classical soliton solutions of the KdV equation.

$$u_t + \left(\frac{u^2}{2}\right)_x + \epsilon u_{xxx} = 0. \tag{7.5}$$

7.1 | Single Soliton Propagation

In the case of a single soliton, the initial condition is as follows,

$$u(x, 0) = 3c\text{sech}^2(k(x - x_0)), \quad x \in [0, 2], \tag{7.6}$$

with $k = 0.5\sqrt{\frac{c}{\epsilon}}$, $c = 0.3$, $x_0 = 0.5$ and $\epsilon = 5 \times 10^{-4}$. The exact solution is a solitary wave (a *soliton*) traveling to the right with speed c, expressed as

$$u(x, t) = 3c\ \text{sech}^2\big(k\big[(x - x_0) - ct\big]\big).$$

The numerical simulations are carried out on the domain $x \in [0, 2]$ with $N = 80$. Figure 8 shows the numerical solution and corresponding error at times $t = 0, 1, 2$, and 3. The TDCCS scheme achieves significantly smaller absolute errors than TDCNCS, resulting in at least an order of magnitude improvement in accuracy.

7.2 | Double Soliton Collision

For the case of a double soliton collision, the initial condition is

$$u(x, 0) = 3c_1\text{sech}^2(k_1(x - x_1)) + 3c_2\text{sech}^2(k_2(x - x_2)), \quad x \in [0, 2], \tag{7.7}$$

with $k_j = 0.5\sqrt{\frac{c_j}{\epsilon}}$ for $j = 1, 2$, $c_1 = 0.3$, $c_2 = 0.1$, $x_1 = 0.4$, $x_2 = 0.8$ and $\epsilon = 4.84 \times 10^{-4}$. The simulations are carried out on the domain $x \in [0, 2]$ with $N = 100$ for times $t \in [0, 4]$. Figure 9 presents the solutions at $t = 0, 1, 2$ together with a contour plot up to $t = 4$. Both TDCNCS and TDCCS perform well for this example.

7.3 | Triple Soliton Splitting

For the case of triple soliton splitting, the initial condition is given by

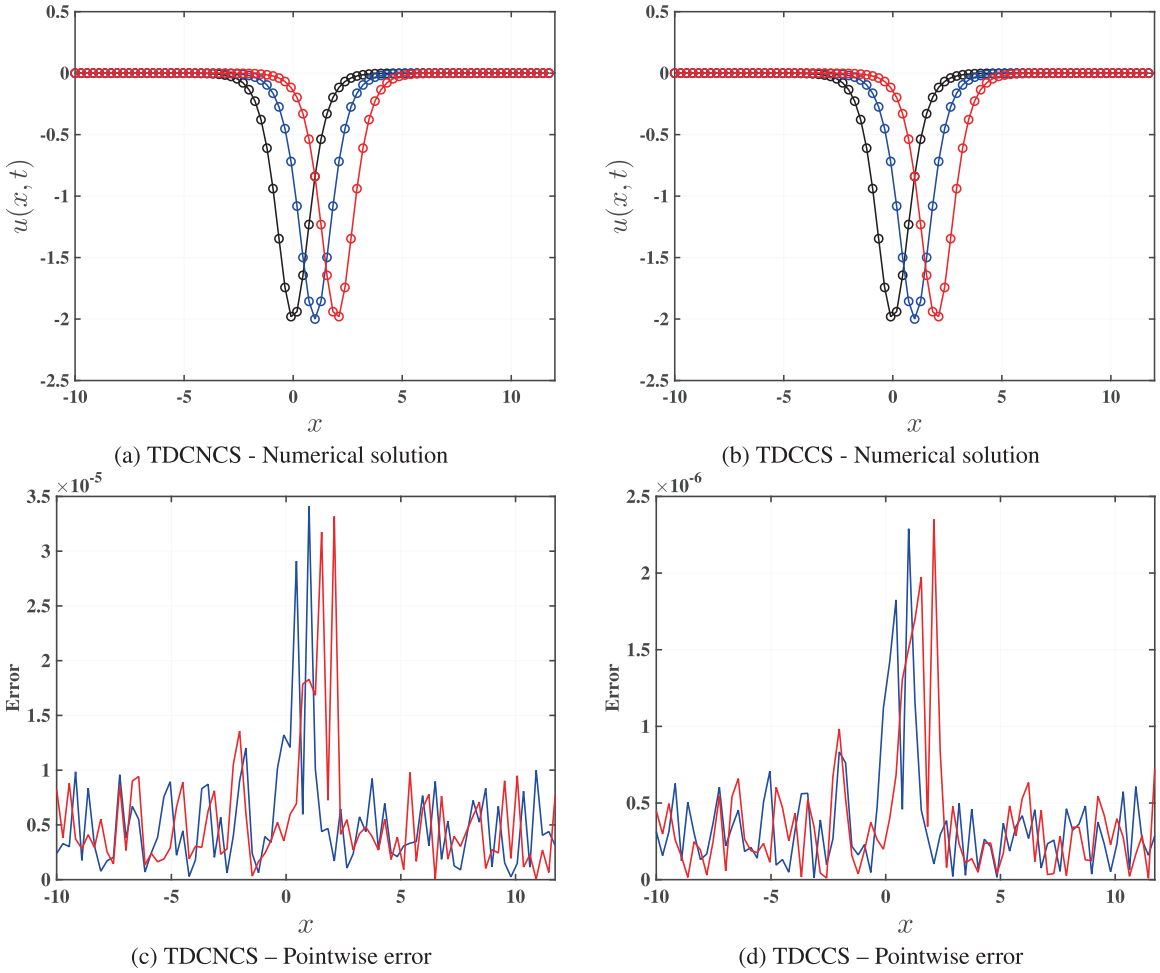

(a) TDCNCS - Numerical solution (b) TDCCS - Numerical solution

(c) TDCNCS – Pointwise error (d) TDCCS – Pointwise error

FIGURE 7 | Numerical results for Example 7.2. The first and second columns correspond to TDCNCS and TDCCS, respectively. The top row shows the exact solution (solid lines) and the numerical approximation (○) at $t = 0$ (black), $t = 0.25$ (blue), and $t = 0.5$ (red). The bottom row displays the corresponding pointwise errors for $N = 80$.

TABLE 10 | Errors and spatial orders of convergence for Example 7.2 at $t = 0.5$.

Scheme	N	L^∞-error	Rate	L^1-error	Rate	L^2-error	Rate
TDCNCS	20	5.4860e-01	—	1.4320e-01	—	2.1960e-01	—
	40	1.3000e-02	5.3992	3.6000e-03	5.3139	4.4000e-03	5.6412
	60	3.2815e-04	9.0741	5.7717e-05	10.1936	8.2161e-05	9.8176
	80	3.3170e-05	7.9665	5.6579e-06	8.0731	7.9961e-06	8.0983
	100	5.6879e-06	7.9021	9.0301e-07	8.2237	1.2950e-06	8.1582
	120	1.3255e-06	7.9889	2.0603e-07	8.1050	2.9640e-07	8.0877
	140	3.7699e-07	8.1565	5.8893e-08	8.1239	8.4988e-08	8.1038
	160	1.2705e-07	8.1452	2.0016e-08	8.0819	2.8873e-08	8.0850
TDCCS	20	2.0500e-02	—	4.3000e-03	—	6.8000e-03	—
	40	2.6299e-04	6.2845	4.7855e-05	6.4895	7.2470e-05	6.5520
	60	1.7387e-05	6.6994	2.9117e-06	6.9043	4.2310e-06	7.0061
	80	2.3505e-06	6.9559	3.8803e-07	7.0057	5.7107e-07	6.9614
	100	4.8863e-07	7.0393	8.2312e-08	6.9487	1.1755e-07	7.0835
	120	1.3224e-07	7.1686	2.2018e-08	7.2326	3.1553e-08	7.2136
	140	4.2387e-08	7.3809	7.1749e-09	7.2739	1.0301e-08	7.2619
	160	1.7577e-08	6.5921	3.0422e-09	6.4255	4.2291e-09	6.6670

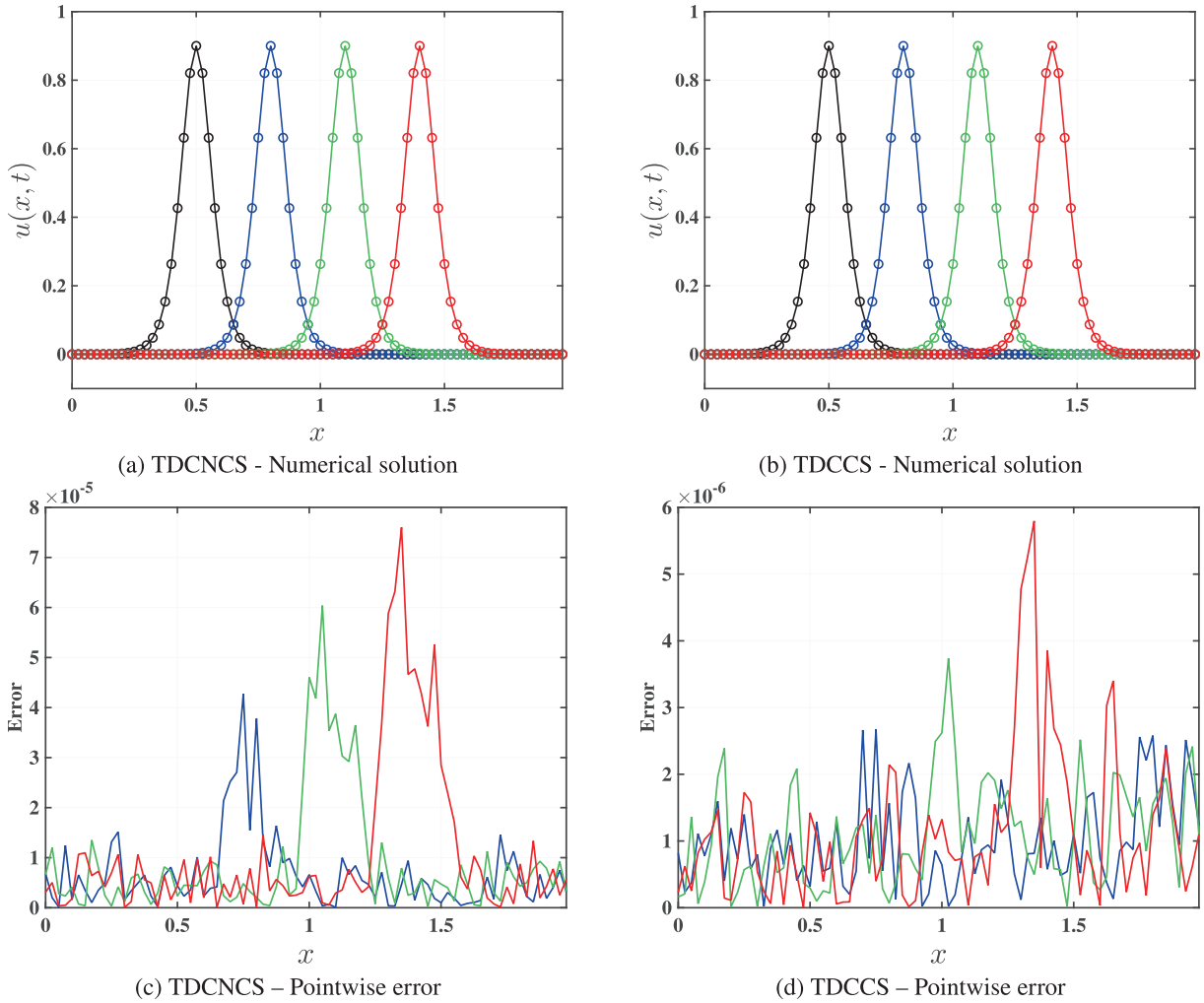

FIGURE 8 | Numerical results for initial condition 7.6 of Example (7.3). The first and second columns correspond to TDCNCS and TDCCS, respectively. The top row shows the exact solution (solid lines) and the numerical approximation (○) at $t = 0$ (black), $t = 1$ (blue), $t = 2$ (green), and $t = 3$ (red). The bottom row displays the corresponding pointwise errors as they evolve over time.

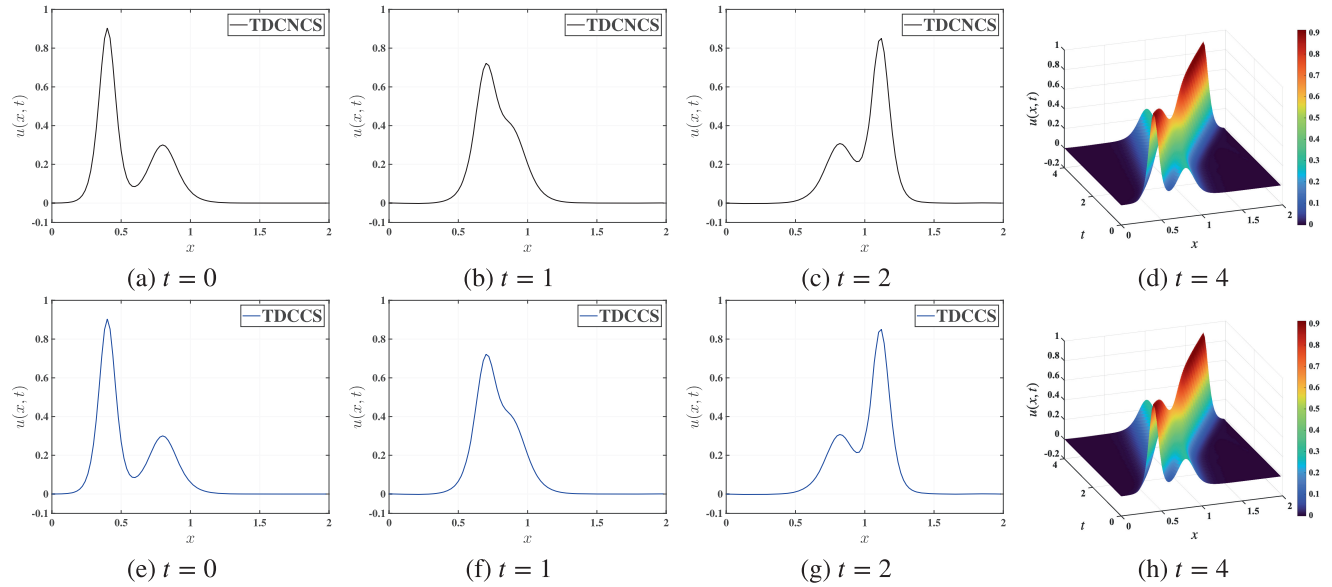

FIGURE 9 | Numerical results for initial condition (7.7) of Example 7.3. The top row shows the solutions obtained using TDCNCS, while the bottom row shows those obtained using TDCCS.

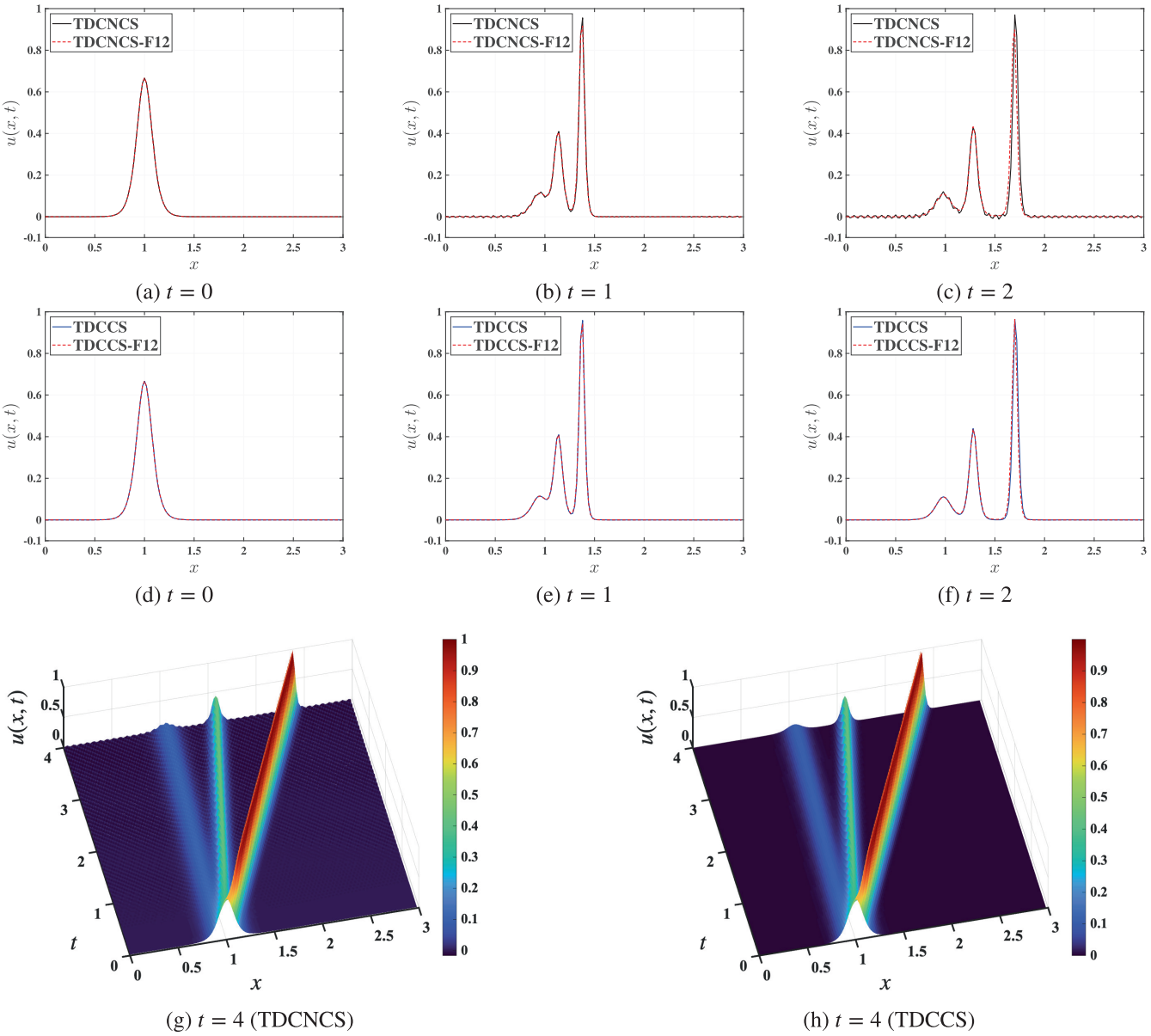

FIGURE 10 | Numerical results for initial condition (7.8) of Example 7.3. The top row shows solutions obtained using TDCNCS with a filter (red) and without a filter (black), while the middle row shows results from TDCCS with a filter (red) and without a filter (blue). The bottom row displays the surface plot at $t = 4$ without a filter.

$$u(x,0) = \frac{2}{3}\operatorname{sech}^2\left(\frac{x-1}{\sqrt{108\epsilon}}\right), \quad x \in [0,3], \tag{7.8}$$

with $\epsilon = 10^{-4}$. Numerical experiments are performed on the domain $x \in [0, 3]$ using $N = 150$ grid points. Figure 10 shows the solutions at $t = 0, 1, 2$ together with a surface plot up to $t = 4$.

Without filtering, the TDCNCS scheme produces noticeable high-frequency oscillations during the soliton splitting process, while the TDCCS scheme yields a comparatively smooth solution. To suppress these oscillations, a 12th-order periodic filter (denoted by F12) with free parameter $\alpha = 0.4$ is applied. The filter is implemented every 20 steps for TDCNCS and every 50 steps for TDCCS.

The numerical results in Figure 10 highlight the effect of filtering on both schemes. In the case of TDCNCS, the unfiltered solution develops oscillations that grow in magnitude after $t = 1$, whereas the filtered solution (TDCNCS-F12) remains much closer to the expected soliton profile. For TDCCS, the unfiltered solution already remains relatively smooth, and the filtered counterpart (TDCCS-F12) introduces only minor corrections. Filtering every 50 steps proves sufficient for TDCCS, but the same frequency of application does not fully eliminate oscillations in TDCNCS, which requires more frequent filtering.

These observations confirm that TDCCS provides a more stable and accurate numerical approximation for soliton splitting, while TDCNCS can achieve comparable accuracy only when combined with frequent high-order filtering.

Example 7.4. In this example, we investigate the zero dispersion limit of conservation laws, specifically the KdV equation (7.3) with the continuous initial condition

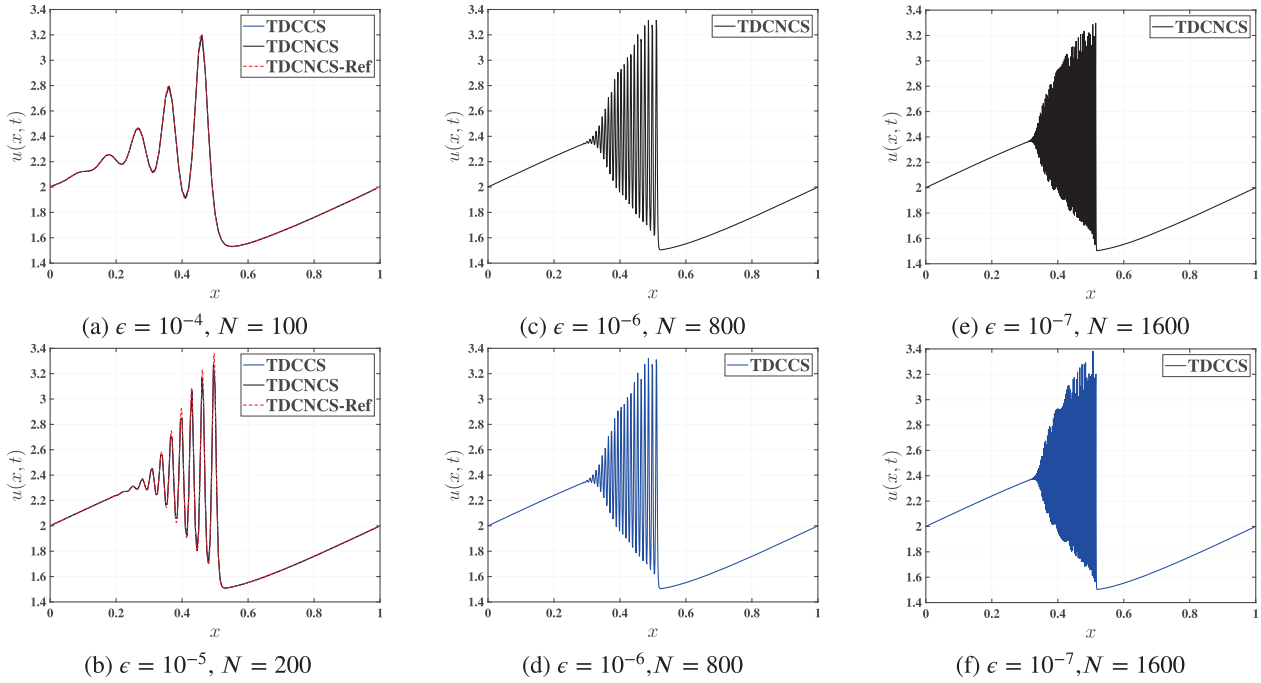

(a) $\epsilon = 10^{-4}$, $N = 100$ (c) $\epsilon = 10^{-6}$, $N = 800$ (e) $\epsilon = 10^{-7}$, $N = 1600$

(b) $\epsilon = 10^{-5}$, $N = 200$ (d) $\epsilon = 10^{-6}$,$N = 800$ (f) $\epsilon = 10^{-7}$,$N = 1600$

FIGURE 11 | Numerical solutions for initial condition (7.9) of Example 7.3 at $t = 0.5$, computed using TDCNCS (black) and TDCCS (blue).

$$u(x, 0) = 2 + \frac{1}{2}\sin(2\pi x), \quad x \in [0, 1]. \tag{7.9}$$

Theoretical and numerical studies of this limit as $\epsilon \to 0^+$ are available in References [27, 28]. Our objective is to evaluate the capability of the proposed methods to resolve fine-scale oscillatory structures that arise when ϵ is small. Solutions are computed at $t = 0.5$ for $\epsilon = 10^{-4}, 10^{-5}, 10^{-6}$, and 10^{-7}. Since no closed-form solution is available, a reference solution is generated using TDCNCS with a highly refined mesh of $N = 1000$. For $\epsilon = 10^{-4}$ with $N = 100$ and $\epsilon = 10^{-5}$ with $N = 200$, Figure 11a,b presents the results from TDCNCS (black) and TDCCS (blue), compared against the reference (red). For $\epsilon = 10^{-6}$ with $N = 800$ and $\epsilon = 10^{-7}$ with $N = 1600$, the results shown in Figure 11c–f can be regarded as *converged* solutions, in the sense that further refinement does not alter the numerical solution. These solutions display persistent oscillatory structures that are characteristic of dispersive limits [28].

It is important to note that these oscillations are physical rather than numerical artifacts. Applying a low-pass filter does not affect the results, since the rapidly oscillating structures of the physical solution are not considered spurious high-frequency noise at the $2\Delta x$ scale when sufficiently fine meshes are employed. However, if the mesh resolution is inadequate, the computed solution may fail to converge. For example, with $\epsilon = 10^{-6}$, simulations using 200, 300, 400, or even 600 cells did not match the converged solution obtained with 800 cells. As $\epsilon \to 0^+$, the numerical problem becomes more difficult, with the required mesh resolution increasing rapidly to capture the small-scale dispersive features.

We now consider the discontinuous top-hat initial condition

$$u(x, 0) = \begin{cases} 1, & \text{if} \quad 0.25 < x < 4, \\ 0, & \text{else}, \end{cases} \tag{7.10}$$

with parameters $N = 1000$, $\epsilon = 10^{-4}$, and evolution times $t = 0.01$ and $t = 0.05$. The corresponding results are shown in Figure 12. For the TDCNCS scheme (top row), the numerical solutions exhibit spurious oscillations around the discontinuity in addition to the left-propagating dispersive wave. These non-physical oscillations are effectively removed after applying a 12th-order filter (F12), as illustrated in subfigures (b) and (d). The filtered results clearly capture the left-propagating wave packet with improved smoothness.

For the TDCCS scheme (bottom row), the unfiltered solutions (subfigures (e) and (g)) already display reduced oscillations compared to TDCNCS, although small irregularities remain near the discontinuity. Application of the same 12th-order filter (subfigures (f) and (h)) further suppresses these oscillations, yielding smooth profiles comparable to those obtained with filtered TDCNCS.

These results demonstrate that the high-order filter successfully eliminates spurious high-frequency oscillations while preserving the dispersive wave structures. The filtered solutions obtained using both TDCNCS and TDCCS are consistent with earlier studies [19, 29], which reported the evolution of the top-hat profile into a sequence of dispersive waves that gradually separate into solitary waves as time increases.

Example 7.5. We consider the two-dimensional linear dispersion equation

$$u_t + u_{xxx} + u_{yyy} = 0, \quad (x, y, t) \in (0, 2\pi) \times (0, 2\pi) \times (0, T], \tag{7.11}$$

with initial condition $u(x, y, 0) = \sin(x + y)$. The corresponding exact solution is $u(x, y, t) = \sin(x + y + 2t)$. Figure 13 presents the numerical solution and pointwise error for $N = 40$ at $t = 1$, while Table 11 summarizes the L^∞-, L^1-, and L^2-errors along

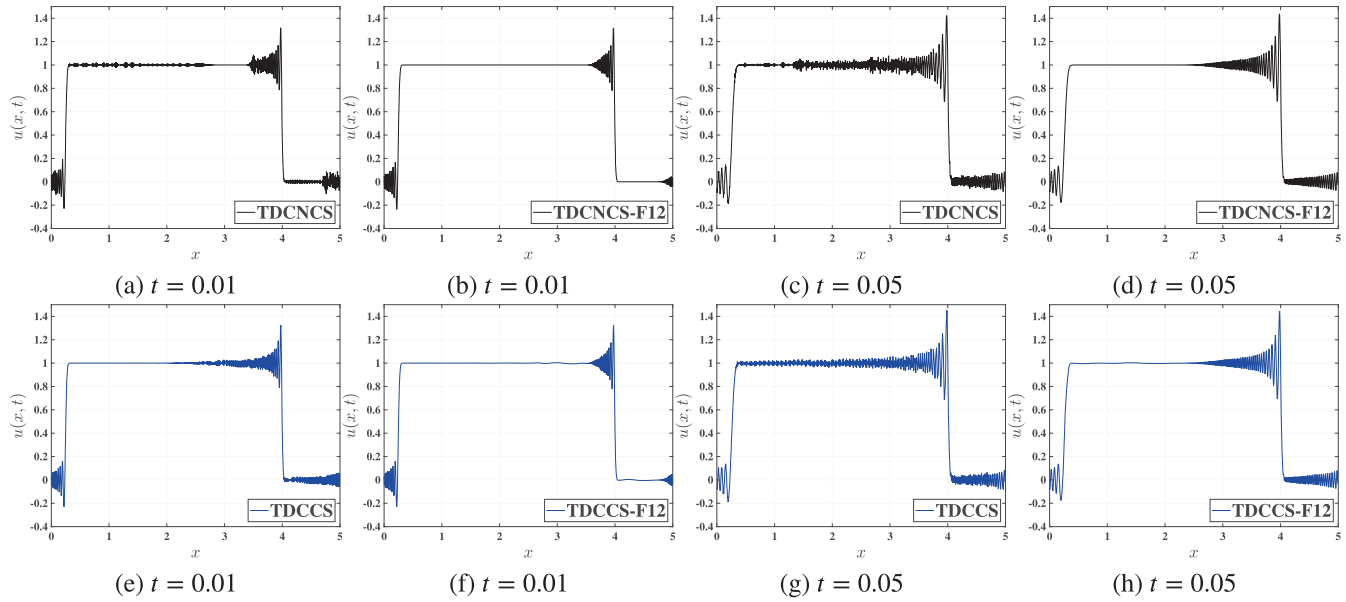

FIGURE 12 | Numerical solutions for initial condition (7.10) of Example 7.3, computed using TDCNCS (black) and TDCCS (blue).

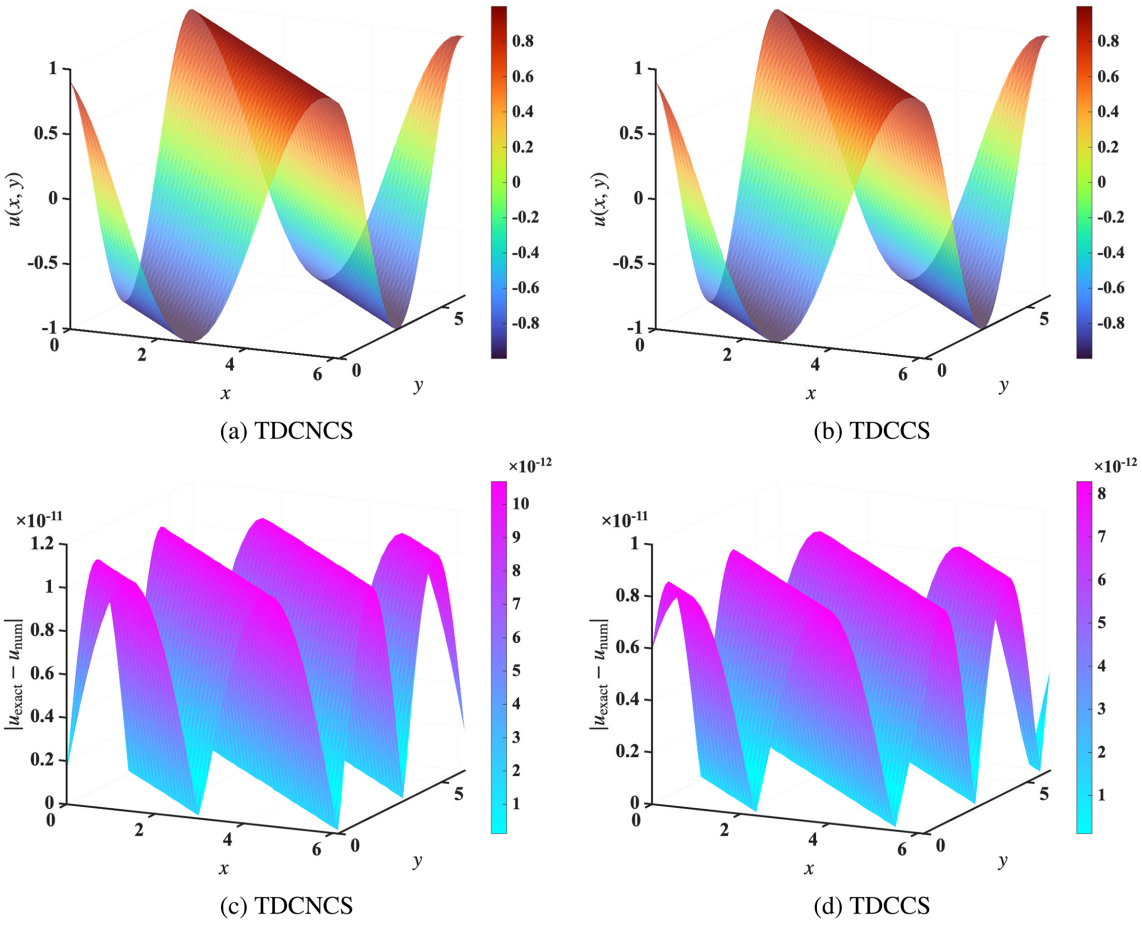

FIGURE 13 | Solutions and errors of Example 7.6. The first and second columns correspond to TDCNCS and TDCCS, respectively. The top row shows the numerical solutions at $t = 1$ with $N = 40$, while the bottom row presents the corresponding errors.

TABLE 11 | Errors and spatial orders of convergence for Example 7.6 at $t = 1$.

Scheme	N	L^∞-error	Rate	L^1-error	Rate	L^2-error	Rate
TDCNCS	10	8.6153e-07	—	5.5759e-07	—	6.1314e-07	—
	15	3.2458e-08	8.0864	2.0701e-08	8.1226	2.3056e-08	8.0911
	20	3.2016e-09	8.0516	2.0581e-09	8.0241	2.2787e-09	8.0447
	25	5.3720e-10	7.9995	3.4221e-10	8.0402	3.7988e-10	8.0285
	30	1.2351e-10	8.0629	7.8764e-11	8.0570	8.7802e-11	8.0340
	35	3.4686e-11	8.2386	2.2075e-11	8.2517	2.4525e-11	8.2737
	40	1.0682e-11	8.8202	6.7786e-12	8.8419	7.5369e-12	8.8360
TDCCS	10	2.4044e-07	—	1.5561e-07	—	1.7125e-07	—
	15	1.1687e-08	7.4581	7.4536e-09	7.4942	8.2985e-09	7.4656
	20	1.2744e-09	7.7030	8.1963e-10	7.6737	9.0735e-10	7.6936
	25	2.2507e-10	7.7700	1.4337e-10	7.8130	1.5915e-10	7.8007
	30	5.3902e-11	7.8391	3.4370e-11	7.8337	3.8200e-11	7.8269
	35	1.7566e-11	7.2734	1.1179e-11	7.2860	1.2422e-11	7.2875
	40	8.2851e-12	5.6279	5.2575e-12	5.6495	5.8456e-12	5.6450

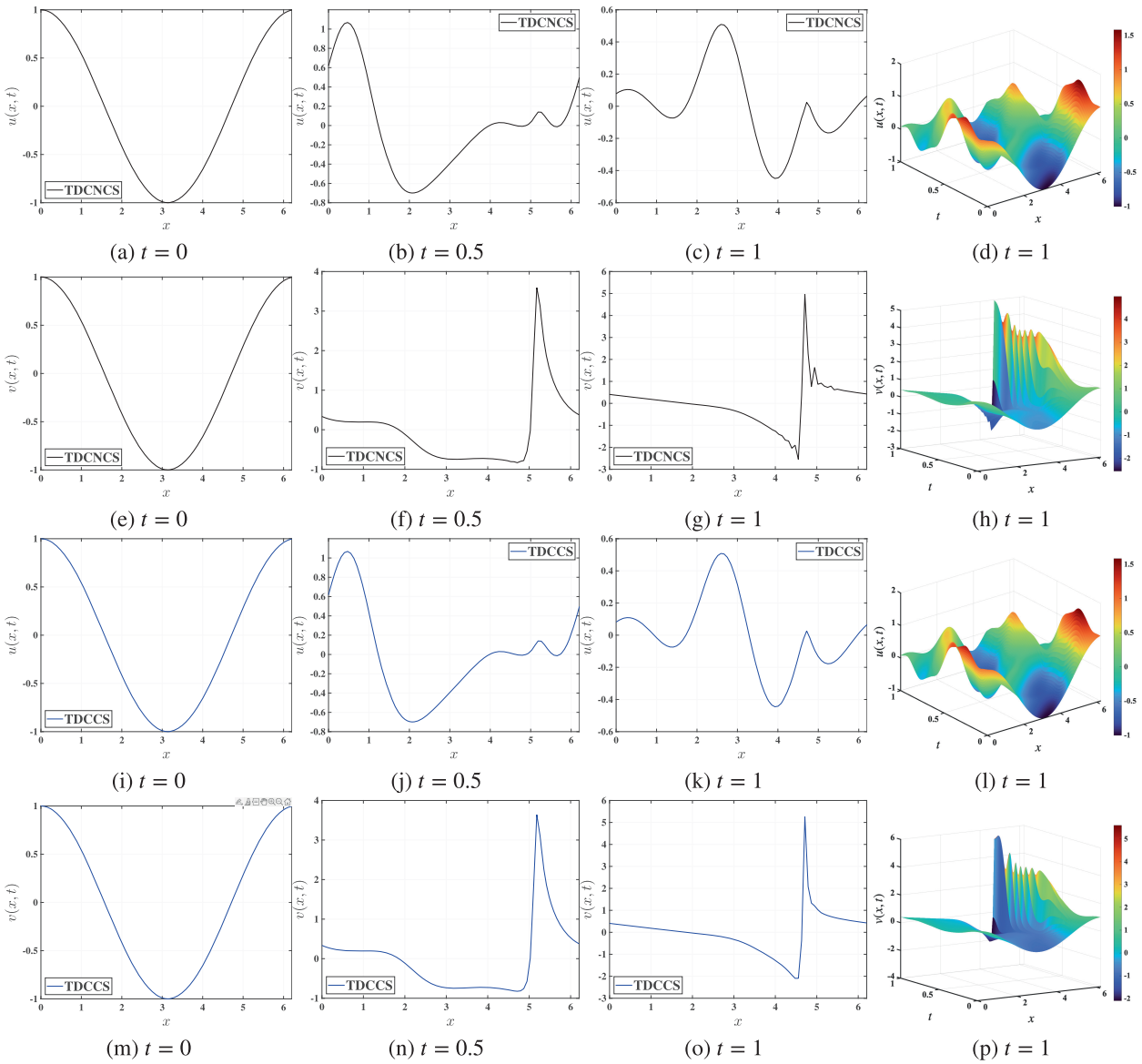

FIGURE 14 | Numerical solutions for initial condition (7.13) of Example (7.12) at $t = 0, 0.5, 1$, computed using TDCNCS (black) and TDCCS (blue).

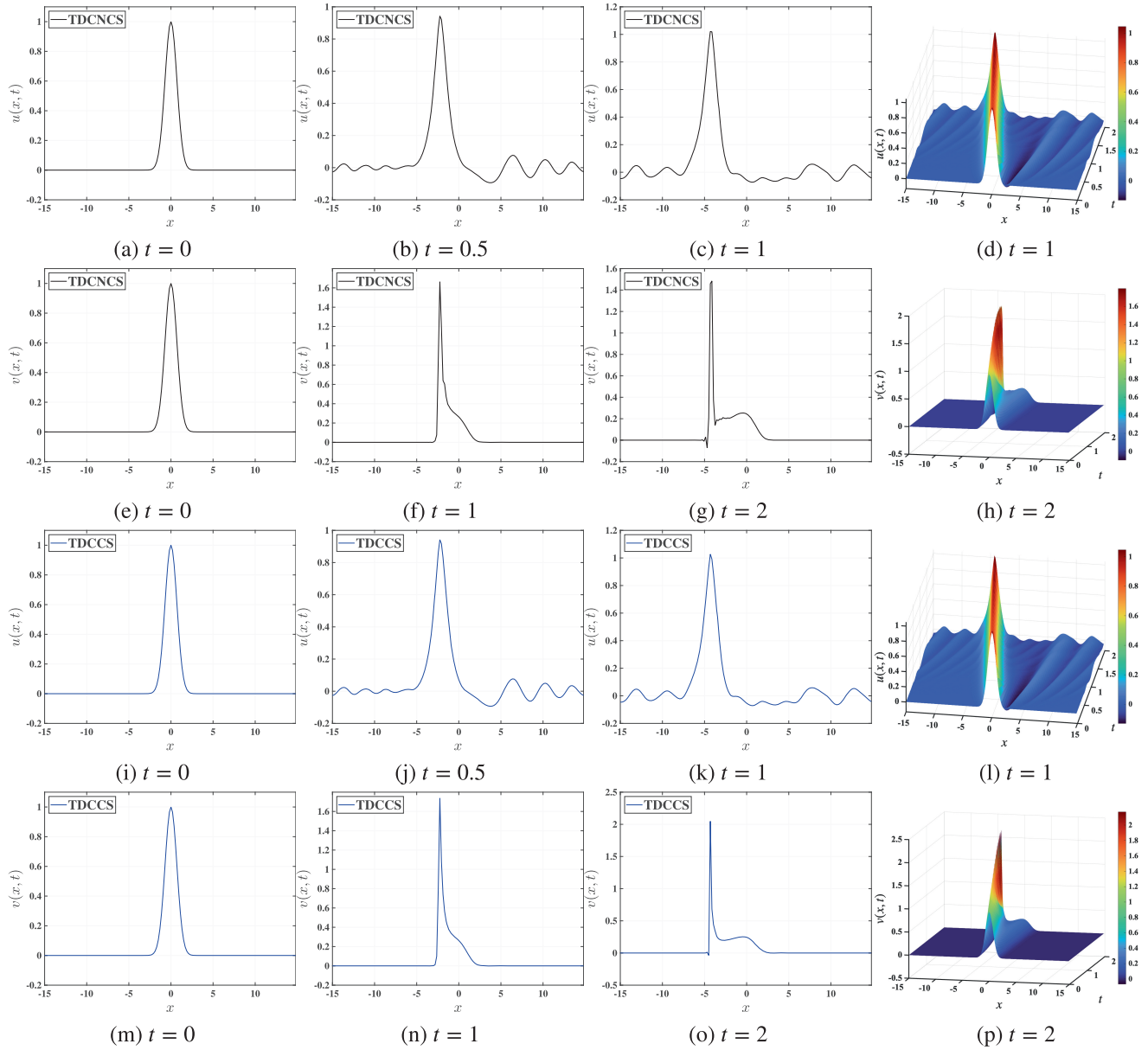

FIGURE 15 | Numerical solutions for initial condition (7.14) of Example (7.12) at $t = 0, 1, 2$, computed using TDCNCS (black) and TDCCS (blue).

with the observed convergence rates at the final time $t = 1$. For instance, the L^∞-error decreases from 3.2016×10^{-9} (TDCNCS) and 1.2744×10^{-9} (TDCCS) at $N = 20$ to 1.0682×10^{-12} and 8.2851×10^{-12}, respectively, at $N = 40$. Further refinement does not reduce the error, as it is limited by machine precision.

Example 7.6. We consider the Ito-type coupled nonlinear problem

$$\begin{aligned} u_t - (3u^2 + v^2)_x - u_{xxx} &= 0, \\ v_t - 2(uv)_x &= 0, \end{aligned} \tag{7.12}$$

with two different initial conditions. First, for the trigonometric case

$$u(x, 0) = \cos(x), \qquad v(x, 0) = \cos(x), \tag{7.13}$$

the simulations are performed with 80 cells in the domain $x \in [0, 2\pi]$ at times $t = 0, 0.5, 1$ under periodic boundary conditions. Figure 14 shows that the u-component exhibits dispersive wave behavior, while the v-component develops shock-type profiles.

Next, for the Gaussian initial condition

$$u(x, 0) = \exp(-x^2), \qquad v(x, 0) = \exp(-x^2), \tag{7.14}$$

the problem is solved with 160 cells in the domain $x \in [-15, 15]$ up to $t = 2$, as shown in Figure 15. A comparison of the two compact schemes shows that TDCCS consistently produces smoother and more stable solutions, particularly in regions with steep gradients, while still preserving the essential dispersive structures. In contrast, while TDCNCS resolves oscillatory features with high accuracy in smooth regions, it tends to introduce mild spurious oscillations near steep gradients. No filtering is applied in these experiments. Overall, TDCCS demonstrates superior robustness for this coupled nonlinear problem, and the computed results align well with those reported in Reference [30].

In summary, the numerical experiments demonstrate that the proposed TDCCS scheme consistently delivers higher accuracy than the reference TDCNCS scheme across a wide range of linear and nonlinear test problems in one and two dimensions, including convection- and dispersion-dominated regimes, thereby confirming its effectiveness and robustness for solving higher-order PDEs.

8 | Conclusions

This paper introduces a new class of compact schemes, termed third derivative central compact schemes (TDCCS), for approximating third-order spatial derivatives in the KdV equation. Additionally, the existing third derivative cell-node compact schemes (TDCNCS) are extended to achieve accuracy up to the tenth order. The TDCCS framework computes third-order derivatives at cell nodes by incorporating values from both cell nodes and cell centers. The values at cell centers are determined using the same scheme as for cell nodes and are treated as independent variables.

A detailed comparison between TDCNCS and TDCCS has been conducted across various scenarios, including the one-dimensional and two-dimensional linear KdV equations, the nonlinear KdV equations, and a convection-dominated problem where the coefficients of the third derivative terms are small.

For linear KdV equations, TDCCS demonstrates significantly lower errors compared to TDCNCS. Specifically, for lower wavenumbers, the errors from TDCCS are at least half of those obtained using TDCNCS, while for higher wavenumbers, TDCCS errors are approximately one-tenth of those from TDCNCS.

For the convection-dominated nonlinear KdV equation, TDCNCS introduces spurious oscillations, requiring the use of a low-pass spatial filter to suppress them. In contrast, TDCCS does not generate spurious oscillations, eliminating the need for filtering. Moreover, wherever the exact solution is available, TDCCS produces errors that are about one-tenth of those from TDCNCS. For continuous convection-dominated problems, neither TDCNCS nor TDCCS requires filtering. However, for discontinuous cases, filtering is necessary to reduce oscillations.

Further tests on two-dimensional linear KdV and coupled nonlinear systems confirm the robustness of the proposed schemes. The linear case highlights the high-resolution capability of TDCCS, while the coupled system demonstrates its stability near steep gradients. Overall, the results indicate that the method remains effective for a wider range of multidimensional and coupled nonlinear PDEs.

In summary, TDCCS provides a more accurate, stable, and efficient alternative to TDCNCS, making it a promising approach for solving third-order derivative problems in KdV equations. Future work will focus on refining the method by incorporating stability-optimized Runge–Kutta techniques to overcome the limitations imposed by a low CFL number.

Acknowledgments

Rathan Samala is supported by NBHM, DAE, India (Reference No. 02011/46/2021 NBHM (R.P.)/R&D II/14874). Debojyoti Ghosh contributed to this article under the auspices of the U.S. Department of Energy by Lawrence Livermore National Laboratory under Contract No. DE-AC52-07NA27344.

Funding

This work was supported by the National Board for Higher Mathematics (Grant No. 02011/46/2021 NBHM (R.P.)/R&D II/14874) and U.S. Department of Energy by Lawrence Livermore National Laboratory (DE-AC52-07NA27344).

Conflicts of Interest

The authors declare no conflicts of interest.

Data Availability Statement

The data that support the findings of this study are available from the corresponding author upon reasonable request.

References

1. S. K. Lele, "Compact Finite Difference Schemes With Spectral-Like Resolution," *Journal of Computational Physics* 103, no. 1 (1992): 16–42.

2. A. M. Wazwaz, *Partial Differential Equations and Solitary Waves Theory* (Springer Science & Business Media, 2010).

3. N. J. Zabusky and M. D. Kruskal, "Interaction of Solitons in a Collisionless Plasma and the Recurrence of Initial States," *Physical Review Letters* 15, no. 6 (1965): 240–243.

4. N. J. Zabusky and C. J. Galvin, "Shallow-Water Waves, the Korteweg-de Vries Equation and Solitons," *Journal of Fluid Mechanics* 47, no. 4 (1971): 811–824.

5. M. Guo, C. Fu, Y. Zhang, J. Liu, and H. Yang, "Study of Ion-Acoustic Solitary Waves in a Magnetized Plasma Using the Three-Dimensional Time-Space Fractional Schamel-KdV Equation," *Complexity* 2018 (2018): 6852548.

6. D. A. Iordache, A. Petrescu, and V. Iordache, "Study of the Solitons Propagation Through Optical Fibers," *UPB Scientific Bulletin A* 72, no. 1 (2010): 53–58.

7. C. L. Gardner, "The Quantum Hydrodynamic Model for Semiconductor Devices," *SIAM Journal on Applied Mathematics* 54, no. 2 (1994): 409–427.

8. F. Q. Hu, M. Y. Hussaini, and J. L. Manthey, "Low-Dissipation and Low-Dispersion Runge–Kutta Schemes for Computational Acoustics," *Journal of Computational Physics* 124, no. 1 (1996): 177–191.

9. R. Hixon and E. Turkel, "Compact Implicit MacCormack-Type Schemes With High Accuracy," *Journal of Computational Physics* 158, no. 1 (2000): 51–70.

10. J. S. Shang, "High-Order Compact-Difference Schemes for Time-Dependent Maxwell Equations," *Journal of Computational Physics* 153, no. 2 (1999): 312–333.

11. M. Lakshmanan, "Solitons, Tsunamis and Oceanographical Applications of," in *Mathematics of Complexity and Dynamical Systems* (Springer, 2012), 1603–1617.

12. P. Karunakar and S. Chakraverty, "Differential Quadrature Method for Solving Fifth-Order KDV Equations," in *Recent Trends in Wave Mechanics and Vibrations: Select Proceedings of WMVC 2018* (Springer, 2019), 361–369.

13. M. J. Ablowitz and P. A. Clarkson, *Solitons, Nonlinear Evolution Equations and Inverse Scattering*, vol. 149 (Cambridge University Press, 1991).

14. A. M. Wazwaz, "The Variational Iteration Method for Rational Solutions for KDV, K(2,2), Burgers, and Cubic Boussinesq Equations," *Journal of Computational and Applied Mathematics* 207, no. 1 (2007): 18–23.

15. D. Levy, C. W. Shu, and J. Yan, "Local Discontinuous Galerkin Methods for Nonlinear Dispersive Equations," *Journal of Computational Physics* 196, no. 2 (2004): 751–772.

16. P. Saucez, A. Vande Wouwer, W. E. Schiesser, and P. Zegeling, "Method of Lines Study of Nonlinear Dispersive Waves," *Journal of Computational and Applied Mathematics* 168, no. 1–2 (2004): 413–423.

17. J. Li and M. R. Visbal, "High-Order Compact Schemes for Nonlinear Dispersive Waves," *Journal of Scientific Computing* 26 (2006): 1–23.

18. M. Ahmat and J. Qiu, "Direct WENO Scheme for Dispersion-Type Equations," *Mathematics and Computers in Simulation* 204 (2023): 216–229.

19. L. V. Salian and R. Samala, "Exponential Approximation Space Reconstruction Weighted Essentially Nonoscillatory Scheme for Dispersive Partial Differential Equations," *Mathematical Methods in the Applied Sciences* 47, no. 4 (2024): 1823–1851.

20. S. Nagarajan, S. K. Lele, and J. H. Ferziger, "A Robust High-Order Compact Method for Large Eddy Simulation," *Journal of Computational Physics* 191, no. 2 (2003): 392–419.

21. B. J. Boersma, "A Staggered Compact Finite Difference Formulation for the Compressible Navier–Stokes Equations," *Journal of Computational Physics* 208, no. 2 (2005): 675–690.

22. S. Zhang, S. Jiang, and C. W. Shu, "Development of Nonlinear Weighted Compact Schemes With Increasingly Higher Order Accuracy," *Journal of Computational Physics* 227, no. 15 (2008): 7294–7321.

23. X. Liu, S. Zhang, H. Zhang, and C. W. Shu, "A New Class of Central Compact Schemes With Spectral-Like Resolution I: Linear Schemes," *Journal of Computational Physics* 248 (2013): 235–256.

24. Z. Wang, J. Li, B. Wang, Y. Xu, and X. Chen, "A New Central Compact Finite Difference Scheme With High Spectral Resolution for Acoustic Wave Equation," *Journal of Computational Physics* 366 (2018): 191–206.

25. S. Gottlieb and C. W. Shu, "Total Variation Diminishing Runge-Kutta Schemes," *Mathematics of Computation* 67, no. 221 (1998): 73–85.

26. E. J. Kubatko, B. A. Yeager, and D. I. Ketcheson, "Optimal Strong-Stability-Preserving Runge–Kutta Time Discretizations for Discontinuous Galerkin Methods," *Journal of Scientific Computing* 60 (2014): 313–344.

27. S. Venakides, "The Zero Dispersion Limit of the Korteweg-de Vries Equation With Periodic Initial Data," *Transactions of the American Mathematical Society* 301, no. 1 (1987): 189–226.

28. P. D. Lax, C. D. Levermore, and S. Venakides, "The Generation and Propagation of Oscillations in Dispersive Initial Value Problems and Their Limiting Behavior," in *Important Developments in Soliton Theory* (Springer, 1993), 205–241.

29. A. Mazaheri, M. Ricchiuto, and H. Nishikawa, "A First-Order Hyperbolic System Approach for Dispersion," *Journal of Computational Physics* 321 (2016): 593–605.

30. Y. Xu and C. W. Shu, "Local Discontinuous Galerkin Methods for the Kuramoto–Sivashinsky Equations and the Ito-Type Coupled KDV Equations," *Computer Methods in Applied Mechanics and Engineering* 195, no. 25–28 (2006): 3430–3447.